



Facile synthesis of precious metal-free Ti-Cu nano-catalyst for enhanced hydrogen and liquid fuels production from in-situ pyrolysis-catalytic steam reforming reaction of polystyrene waste dissolved in phenol

Walid Nabgan ^{a,*}, H. Alqaraghuli ^b, B. Nabgan ^c, T.A. Tuan Abdullah ^{d,*}, M. Ikram ^{e,*}, F. Medina ^a, Ridha Djellabi ^a

^a Departament d'Enginyeria Química, Universitat Rovira i Virgili, Av Països Catalans 26, 43007, Tarragona, Spain

^b Faculty of Electrical Engineering, Universiti Teknologi Malaysia, 81310 Skudai, Johor, Malaysia

^c School of Chemical and Biomolecular Engineering, The University of Sydney, Sydney, NSW, 2006, Australia

^d Faculty of Chemical and Energy Engineering, Universiti Teknologi Malaysia, 81310 Skudai, Johor, Malaysia

^e Solar Cell Applications Research Lab, Department of Physics, Government College University Lahore, 54000, Punjab, Pakistan



ARTICLE INFO

Keywords:
Non- noble
Polystyrene
Plastic
Waste

ABSTRACT

In-situ pyrolysis-catalytic steam reforming reaction of polystyrene waste (PSW) liquefied in phenol can generate hydrogen from phenol and valuable liquid fuel from the PSW and thus has been studied recently. However, due to the complexity of phenol compounds and plastic waste, this reaction suffers from high energy consumption and coking. Herein, Ti, 4Ti3Cu and 3Ti3Cu nano-catalysts were facilitatively prepared using hydrothermal and impregnation methods and the physical and chemical properties of the fresh and used samples were deeply characterized. The experimental results show that almost complete phenol conversion with 97.90% H₂ yield was achieved at 800 °C using 3Ti3Cu nano-catalyst. The catalytic pyrolysis products were ethylamine, tert-butyl hydroperoxide (TBHP) and benzene (1,1-dimethylethoxy) (BDE). The correspondence of the preparation, morphology and catalytic activity in this research elucidates the synthesis of anti-coking and stable nano-catalysts for in-situ pyrolysis-catalytic steam reforming reaction.

1. Introduction

Since the 1950s, the amount of municipal waste generated by the manufacturing sector and home consumption has been increasing faster due to the expanding population and increased human activities. Common municipal waste includes plastics, used tires, old clothing, kitchen waste, paper, etc. [1]. The average weight of waste plastic, the polymerization or polycondensation of monomers, creates macromolecular; it makes up 10% of the annual worldwide trash production [2]. One of the essential plastic wastes is PSW, which makes a wide range of consumer goods. The petroleum sector typically provides the monomers, as in the case of the ethylene-based synthesis of PSW. Therefore, the production of polyethylene, polypropylene, polystyrene, polyethylene terephthalate, polyvinyl alcohol, and polyvinyl chloride has increased more than other plastics. PSW plastic is frequently used in items that demand clarity, such as food packaging and laboratory equipment, as it

is a complex, solid plastic. Recent scientific reports claim that 7–8 billion tons of solid waste are created annually around the globe, posing a significant problem for the scientific community due to the numerous negative impacts on the environment and human health [3]. In waste-to-energy plants, very little of the plastic that we discard every day gets recycled. A large portion of it is disposed of in landfills, where it might take up to 1000 years to degrade and release potentially harmful materials into the soil and water. Burning, another way to dispose of plastic waste, is detrimental to the environment since burning releases hazardous chemicals into the air. Thus, finding the right recycling solution is necessary since burning and burying plastic waste plastic is extremely harmful to the environment.

In view of this scenario, waste plastic treatment means must be applied to improve their valorization rate. The thermochemical methods are among the most promising for application, and growing interest is being shown in the thermal treatment alternatives of pyrolysis, steam

* Corresponding authors.

E-mail addresses: walid.nabgan@urv.cat (W. Nabgan), tuanamran@utm.my (T.A. Tuan Abdullah), dr.muhammadikram@gcu.edu.pk (M. Ikram), ridha.djellabi@yahoo.com (R. Djellabi).

reforming, and combined pyrolysis/reforming systems as feasible alternative environmental and financial solutions for plastic waste processing. Compared to landfilling or conventional waste incineration, the in-situ pyrolysis-catalytic steam reforming reaction method provides various benefits, such as conversion plastic wastes and producing H₂ and liquid fuels rather than harming the environment. Accordingly, recycling of PSW is substantial for environmental remediation and moves towards a more circular plastic economy. Pyrolysis manages plastic waste sustainably while producing solid char, gases, and liquid oil as energy sources [4]. Complex compounds or long-chain hydrocarbons are thermally broken down into simpler molecules or shorter-chain hydrocarbons. Additionally, using raw bio-oil from pyrolysis is difficult since it has a high oxygen concentration that concurrently lowers its energy content [5]. Furthermore, PSW temperatures seldom reach the levels required for thermal deterioration; hence this phenomenon is uncommon [6]. As a result, dissolving PSW in a dissolving agent may be a great answer to PSW problems and the creation of clean and renewable energy. As previously investigated [7,8], phenol is an effective dissolving agent since it is acidic to certain plastics, rubber, aluminium, its alloys, and lead. Phenolic constituents often result from the production of petrochemical by-products [9] and makeup around 38% of the unwanted pyrolysis oil ingredient [10]. In addition to the practical liquid fuel generation, the employment of phenol can also allow H₂ generation from in situ pyrolysis-catalytic steam reforming reaction. The chemical H₂ is essential for many industrial processes and may one day serve as a source of clean energy. Thus, using PSW plastics as feedstocks for valuable liquid goods and phenol as a source for chemicals like H₂ will encourage the recycling of plastic waste, stop the difficulties created by the waste plastics, and act as an alternative supply of chemicals, enabling a circular economy.

In the pyrolysis-catalytic steam reforming reaction, catalysts are frequently employed to improve product dispersion and raise product selectivity. At the in-situ catalytic pyrolysis processes, the catalyst and feedstock are mixed, and the pyrolysis and vapour catalytic reforming/ cracking processes take place in the same reactor; therefore, the capital and operating costs are reduced. Additionally, catalysts have been used to upgrade pyrolysis products such that the hydrocarbon distribution is improved and has characteristics comparable to traditional fuels like diesel and gasoline [11,12]. For the sustainable production of H₂ and liquid fuel, large-scale commercial use of noble metals such as Pd [13–15], Rh [16,17], and Pt [18,19] was employed and demonstrated the best catalytic activities; however, they are prohibitively costly. As an alternative, lots of studies on the design of non-precious metal-based catalysts for the H₂ generation, such as bimetallic Ni-Co [10,20–24], Al [25,26], and Fe [27,28], have been investigated. In contrast, significant challenges such as unstable changes in morphology after the reaction, low stability, and selectivity remain. Specifically, as appealing substitutes to traditional noble metal-based catalysts, noble metal-free catalysts could have a promising future in initiating reforming and cracking reactions. Recently, the Ti@TiO₂ core-shell nanoparticles were stated as a precious metal-free photocatalyst for the photothermal H₂ production from aqueous glycerol solutions [29]. Yancheng et al. [30] used porous copper (Cu) foam as catalyst support for H₂ production from methanol steam reforming reaction. Though its overall efficiency was lower, the microreactor utilizing Cu foam covered with 0.6 g of catalyst had more excellent methanol conversion and H₂ generation rates per catalyst weight than when foams with higher catalyst loading were utilized. The previous investigation on the addition of Cu to Ni/Al₂O₃ catalyst found that low loadings of Cu served to lessen the alloying impact brought on by Cu enrichment, which helped prevent the production of carbon on the catalyst [31]. Additionally, it has been claimed that the low-valence Cu species (Cu⁰ or Cu⁺) in the majority of Cu catalysts are active species [32]. Developing and preparing effective precious metal-free catalysts for H₂ production from the in-situ pyrolysis-catalytic steam reforming reaction of PSW dissolved in phenol is the most difficult challenge in this sector. There is a sizable possibility for

carbon to develop and be deposited on the catalyst's surface since this process requires the removal of H₂ from phenol and liquid fuel hydrocarbons from PSW. Therefore, additional precious metal-free catalysts must be developed to present potential candidates as precious metal catalyst substitutes.

To the best of our knowledge, studies are deficient for explaining the effect of the chemical and physical properties on the selectivity and coking resistance of the Ti-Cu nano-catalyst in in-situ pyrolysis-catalytic steam reforming conditions. Herein, we report the facile synthesis and characterization of a precious metal-free Ti-Cu nano-catalyst and their favourable catalytic properties towards H₂ and liquid fuel generation from in-situ pyrolysis-catalytic steam reforming reaction of PSW dissolved in phenol. Catalysts before and after reaction were characterized by several methods correlating their structural and textural characteristics with catalytic activity. In the present work, three precious metal-free nano-catalysts, Ti, 4Ti3Cu (4 g Ti with 3 g Cu) and 3Ti3Cu (3 g Ti with 3 g Cu), were prepared by hydrothermal and impregnation methods to research the influences of Cu addition on the catalytic performance of the catalysts. The crystallinity and synergistic effect of calcined Ti-Cu on the inhibition of materials sintering and the surface area along with pore size distribution of the fresh catalysts were characterized by X-ray diffraction (XRD) and the Brunauer, Emmett and Teller theory (BET), respectively. The basicity study was conducted by the temperature programmed desorption of carbon dioxide (CO₂-TPD), pyrrole-differential thermogravimetric analysis (DTG) curves, and pyrrole-FTIR spectra. Pyridine FTIR spectra and pyridine - DTG curves of the fresh catalysts were used to illustrate the Brønsted and Lewis acid sites. Transmission electron microscopy (TEM) and H₂ temperature-programmed reduction (H₂-TPR) were used to demonstrate the benefits of Cu doping on the dispersion and reducibility of Ti. Fourier-transform infrared spectroscopy-potassium bromide (FTIR-KBr) was used to examine functional groups present in the synthesized catalysts. Catalysts were tested in a fixed-bed reactor that is modified for higher PSW plastic waste to be reacted compared with our previous research [14,33–35], and the optimum catalyst base on the highest phenol conversion and H₂ yield was tested at 500–800 °C and 45 h on stream. The produced liquid product samples were characterized by gas chromatography/mass spectrometry (GC/MS) and FTIR systems. Used catalysts after experiments were also collected and characterized by thermogravimetric analysis (TGA), FTIR-KBr, BET, TEM and CHNS.

2. Materials and methods

2.1. Catalyst preparation

Nano catalysts Ti, 4Ti3Cu, and 3Ti3Cu were synthesized by hydrothermal technique with the Ti to Cu mass ratio of 1, 3:3, and 4:3, respectively. The starting reagents of titanium and copper were titanium (IV) oxide (TiO₂, with the purity of 99.8%) and copper (II) nitrate trihydrate (Cu(NO₃)₂.3H₂O, with the puriss. p.a. grade of 99–104%) which were acquired from Sigma-Aldrich and the synthesis stages are shown in Fig. S1. In accordance with our previous exploration [36,37], nano-sized Ti and Cu catalysts were separately gone through hydrothermal treatment, in which those materials were first stirred with 100 mL of deionized water at room temperature. 5 M of sodium hydroxide (NaOH) was gently dissolved with the solution to improve the nucleation and growth rates of the nanoparticles [38] and stirred for three hours at room temperature to form a clear mixture. Then, the mixture was transferred into a 100 mL Teflon-lined autoclave reactor and was hydrothermally treated at 160 °C for two days. The solid precipitate was repeatedly centrifuged (400 rpm) to separate the solid products from the liquid phase, filtered and washed with deionized water 15 times via filter paper on a Buchner funnel that was sealed with a rubber bung on the top of a side arm conical flask. The side arm of the flask was connected with a vacuum pump to speed the filtration and washing process of the samples, followed by drying at 110 °C overnight and then

calcination for three hours at 800 °C. In order to cure and harden catalysts for industrial use, remove impurities, and drive out chemically bonded moisture, calcination is a crucial step in the process of making catalysts. The prepared nano-sized Ti and Cu particles then went through the conventional impregnation method for synthesizing 4Ti3Cu and 3Ti3Cu. The detail of preparation is explained in our previous research [23,24]. In brief, a specific quantity of the calcined Ti was mixed in 150 mL of deionized water and stirred for an hour at 90 °C, and then the calcined Cu was introduced into the mixture. After vigorous stirring for a few hours, the liquid was evaporated, and a slurry was produced and dried overnight in an oven at 110 °C. Lastly, the acquired dried solid was calcined in an oven (Model Ney Vulcan D-130) at 800 °C for 3 h (30 °C min⁻¹).

2.2. Characterization methods

XRD curves were obtained employing D8 ADVANCE Bruker X-ray diffractometer operated at 40 mA and 40 kV with Cu Ka radiation at 2 theta of 10–100°. The crystalline phases were classified by JCPDS (Joint Committee on Powder Diffraction Standards) using X'Pert Highscore Plus software, and crystal sizes were estimated from diffraction line widths using the Scherrer equation. Nitrogen (N₂) adsorption–desorption performances for fresh and used samples were obtained in a Beckman Coulter SA3100™ apparatus using liquid N₂ at –196 °C. Each catalyst was degassed at 200 °C under a vacuum for 3 h before the adsorption experiments. The BET technique was used to evaluate the specific surface area. At the same time, the average pore size was calculated using the Barrett-Joyner-Halenda (BJH) technique utilizing the adsorption curve to get the total pore volume at relative pressure P/P⁰ = 0.99. The fresh and used TEM images were acquired using a JEOL JEM-1011 microscope that functioned at 80 kV. TEM specimens were equipped by dispersing the catalyst powder in acetone with sonication

and dropping it onto an ultrathin carbon-coated Cu grid. TGA-DTG analysis of the used catalysts was carried out using a Shimadzu TG-50 thermogravimetric analyzer via the flow of N₂ to heat the samples from 30° to 800°C with a heating rate of 20 °C min⁻¹. The H₂-TPR was accomplished on a Micromeritics Chemisorb 2720 apparatus, and the analysis was carried out in a pure H₂ at a flow rate of 30 mL/min, and the temperature was increased from room temperature to 900 °C with a heating rate of 20 °C min⁻¹. CO₂-TPD was also conducted on the same device to detect the basicity of the catalyst. The samples were put into a quartz tube and pretreated in a Helium (He) flow at 250 °C for 1 h and then cooled down to room temperature naturally. The catalyst samples were exposed to the CO₂ environment at 110 °C after the pre-treatment step until their surface sites reached their saturation state. After attaining saturation, the samples were flushed with inert gas He. Further, the temperature was increased to 900 °C with a ramp rate of 20 °C/min to determine the quantity of desorbed CO₂ from the surface basicity sites using a thermal conductivity detector (TCD). The elemental linkage information of the fresh and used samples was studied by FTIR curves detailed via a Shimadzu IR-Prestige-21 model spectrometer using pure KBr as a reference background record with a scanning range of 400–4000 cm⁻¹. The KBr pellet was prepared by mixing the catalyst with KBr with a mass ratio of 100:1, and the excellently prepared combination was pressed to procedure a 13 mm diameter pellet. The same apparatus was used to determine the functional cluster presented in the liquid products in addition to the GC/MS (Agilent 7890B).

2.3. Catalyst performance evaluation

The reaction performance of the prepared Ti, 4Ti3Cu, and 3Ti3Cu was investigated via the combination of a fixed-bed reactor and online mass spectrometry. The case length was 300 mm, and the internal

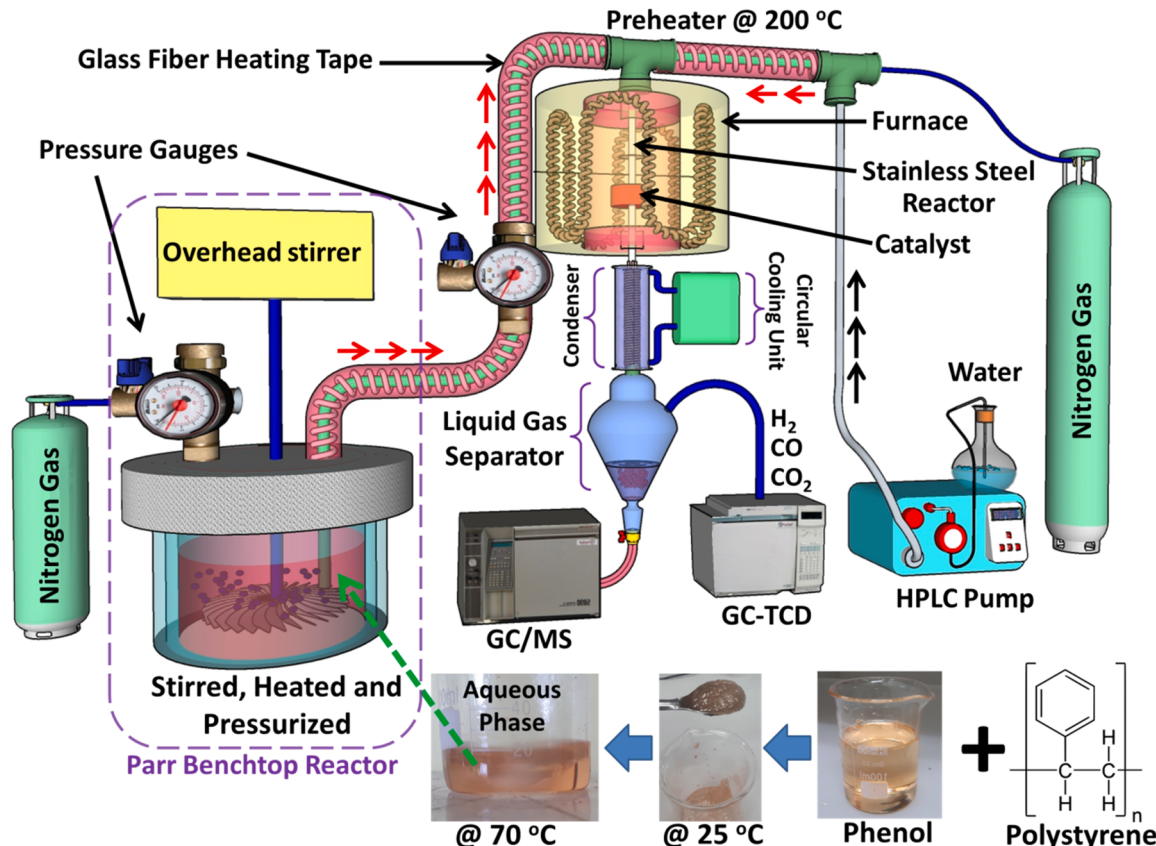


Fig. 1. Diagram of the fixed bed reactor employed in the in-situ pyrolysis-catalytic steam reforming reaction.

diameter was 8 mm at atmospheric pressure; the diagram of the experimental apparatus is illustrated in Fig. 1. 0.2 g of the catalysts were located inside the reactor, and the temperature of the catalyst bed was measured and controlled by a K-type thermocouple, which was linked to a temperature controller. The catalyst was reduced in place for one hour at 600 °C using 30 mL/min of pure H₂ after flushing the catalyst bed with N₂ at 300 °C. The water was fed into the pre-heater using a high-performance liquid chromatography pump (HPLC Bio-Rad™, Series 1350) to inject the fuel with 0.36 mL/min before mixing with carrier N₂ (30 mL/min). In our previous research [14,33–35], we used a very small amount of plastic waste dissolved in phenol to avoid the blockage of the line before the reactor and experimental limitation. To increase the feasibility of the reaction and the amount of plastic waste in the reaction, we modified the experimental rig with a Parr Benchtop Reactor. Herein, the slurry of phenol and PSW plastic with the volumetric ratio of 5:1 was mixed with water vapour molecules and fed to the reactor using a pressurized Parr Benchtop Reactor that kept the PSW-phenol slurry in an aqueous phase at 70 °C, and transfer pipes were swathed using glass fibre heating tape and preheated at 200 °C. With the volumetric ratio of water to PSW-phenol solution of 10:1 with two mass flow controllers individually equipped for phenol line and water line that precisely monitored the flowrates of reactants; the water to PSW-phenol vapour was pumped into the reactor. For activity testing, all catalysts were treated at 500 °C. The optimum catalysts were tested in reaction temperatures ranging from 500 °C to 800 °C with a gap of 100 °C, and the relevant performance results were collected in steady-state situations. Likewise, the constancy examination of the optimum catalyst was conducted at 500 °C for 45 h. After the reactor, a condenser was installed and connected with a circular cooling system at 10 °C to liquefy the condensable liquid molecules, followed by a liquid gas separator. The components present in the gas products were analyzed online employing a GC-TCD (Agilent 6890 N), and the liquid product was analyzed using a GC-FID (HP 5890 Series II) equipped with a 0.53 mm × 30 m CP-Wax capillary column and GC/MS (Agilent 7890B). Each run was repeated at least six times to ensure accuracy and reproducibility. The result analyses, such as phenol conversion, produced gas composition in yield, were calculated following our previous research [14] and as shown in Eqs. (1), (2), (3), and (4).

$$\text{Phenol conversion}(\%) = \frac{[\text{Phenol}]_{\text{in}} - [\text{Phenol}]_{\text{out}}}{[\text{Phenol}]_{\text{in}}} \times 100 \quad (1)$$

$$\text{H}_2\text{ yield}(\%) = \frac{\text{moles of H}_2\text{ obtained}}{\text{moles of H}_2\text{ stoichiometric}} \times 100 \quad (2)$$

$$\text{CO yield}(\%) = \frac{\text{moles of CO obtained}}{\text{moles of CO stoichiometric}} \times 100 \quad (3)$$

$$\text{CO}_2\text{ yield}(\%) = \frac{\text{moles of CO}_2\text{ obtained}}{\text{moles of CO}_2\text{ stoichiometric}} \times 100 \quad (4)$$

The quantity of chemicals that react for the reaction to be fully catalyzed is known as the stoichiometric moles. So, for example, Eq. 5 represents the balancing steam reforming equation.

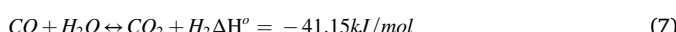
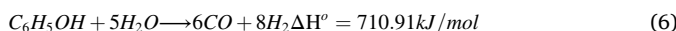


Table 1
BET surface area, pore diameter, pore-volume, reducibility, basicity, and crystal sizes records of the fresh nano-catalysts.

Catalyst	Crystal size (nm)	Surface area (m ² ·g ⁻¹)	Pore-volume (cm ³ ·g ⁻¹)	Pore-diameter (nm)	CO ₂ uptake (μmol·g ⁻¹)	H ₂ -Consumption (mmol·g ⁻¹)
Ti	93.94	15.912	0.0717	18.02	6.48	0.006
4Ti3Cu	71.92	5.374	0.0308	22.93	23.08	15.04
3Ti3Cu	67.68	3.73	0.0216	23.16	78.33	16.80

3. Results and discussion

3.1. Characterization of the fresh catalyst

Table 1 depicts the surface area, pore volume and pore diameter of Ti, 4Ti3Cu, and 3Ti3Cu catalysts, defined by N₂ adsorption–desorption investigation. As can be seen in **Table 1**, introducing Cu causes produce different surface areas, pore sizes and pore volumes. The BET surface area of Ti, 4Ti3Cu, and 3Ti3Cu is 15.912 m²/g, 5.374 m²/g, and 3.73 m²/g, respectively. Obviously, higher Cu contents nano-catalysts cause to decrease in the surface area, partial collapse of ordered mesoporous structure and the rise of the pore diameter (D_p). Typically, in comparison to bare Ti catalyst, 3Ti3Cu catalyst only displayed a surface area of 3.73 m²/g, and its pore volume was low. The sintering of nanoparticles during the calcination process might be significantly delayed by Ti components having a mesoporous structure, preserving a greater specific surface area. This decrease is caused by the inclusion of Cu, which partially covers the catalysts' surfaces and blocks some of their pores. The catalyst made of Cu may be simple to sinter at 600 °C in a reducing atmosphere, which leads to the growth and agglomeration of the active particles and a reduction in the specific surface area [39]. **Fig. 2** displays the pore size distribution and the N₂ isotherms for the fresh catalysts. Ti and 4Ti3Cu isotherms can be categorized as type-IV ascribed to the mesoporous structure [40]. However, the Ti and 4Ti3Cu samples' distribution pore size curve displayed a peak in the area above 50 nm, indicating the presence of macropores in their structure. The 3Ti3Cu material, on the other hand, exhibits a type IV isotherm and an H4 hysteresis curve, both of which are typical of slit-shaped pores [41]. This phenomenon is caused by developing tiny CuO micro crystallites that partially obstruct mesopore access.

The XRD outlines of as-synthesized materials are displayed in **Fig. 3**; estimated crystallite sizes are included in **Table 1**, and the crystal sizes are diverse from 67 to 93 nm for all nano-catalysts. Diffraction peaks are prominently located at about 39.2° (200), 70.6° (122) and 76.5° (202) and marked with blue stars, matched with the standard XRD pattern of rutile Ti₂O₄ (JCPDS, No. 96–900–7433) and match with the crystallite sizes of 80.8 nm. The characteristic diffraction peaks of spinel phases at 20 of 25.7°, 37.5°, 38.4°, and 69.04° were observed (marked with red hearts) and can be ascribed to representative peaks of (101), (103), (004), and (116) crystal phases and corresponding to the JCPDS number of 96–101–0943 for anatase Ti₄O₈, and equal with the crystal size of 42.3 nm. Meanwhile, the peaks appearing at 48.6°, 54.3°, 55.7°, 63°, 75.9° and 82.9° could be assigned to the characteristic peaks of 202, 023, 151, 061, 151 and 402 crystal phases and correspond to the JCPDS number of 96–900–9088 for orthorhombic phase structure of brookite Ti₈O₁₆, and correspond with the crystallite size of 98.2 nm. After introducing CuO to the TiO₂, multiple new diffraction peaks for the tenorite (Cu₄O₄) (JCPDS, No. 96–110–0029) were detected (marked with green trefoil shapes) at 35.6°, 49.1°, 58.7°, 61.9°, 66.1°, and 72.9° which could be assigned to the diffraction peaks of 002, 202, 202, 113, 022 and 311 monoclinic phase structures, respectively, and equal to the crystallite size of 47 nm. The decrease in intensities after introducing the CuO to TiO₂ reveals that the Cu is highly dispersed in the catalysts or causes a crystal size reduction. The XRD patterns of 4Ti3Cu and 3Ti3Cu catalyst resulted in two more new peaks at 20 of 27.6 and 68.6, consistent with 110 and 126 crystal planes, which can be attributed to the monoclinic [JCPDS 96–153–9683] structure of TiO₂ and marked

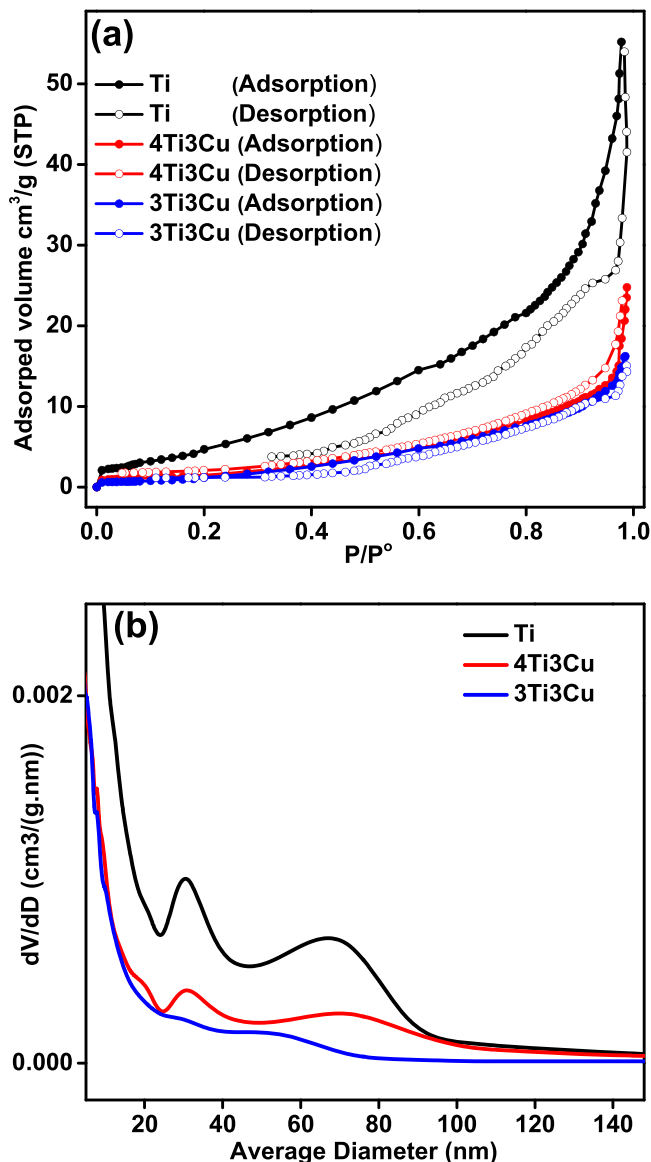


Fig. 2. (a) N_2 adsorption and desorption isotherms and (b) pore size distribution of the fresh samples.

with purple triangles (~ 70 nm). The catalysts synthesized by the hydrothermal method showed in addition to obvious copper oxide and titanium dioxide phases, the bimetallic oxide catalyst Cu-Ti was also successfully synthesized in this experiment. This phenomenon can be approved by the appearance of the peak with the blue circle at 32.9° (~ 60.6 nm) and can also be attributed to the diffraction peaks of 101 tetragonal phase structures of CuTi_3 alloy. However, for the 3Ti3Cu catalyst, the diffraction peaks' intensity is low, meaning that the Ti might be highly dispersed on the Cu. It might be the "combustion" process that gives the catalyst with enhanced Ti dispersion and smaller crystal sizes. Considering the low intensity of XRD peaks of the 3Ti3Cu catalyst, one can say that Ti and Cu are present mainly in the amorphous phase in the synthesized catalysts. This also could suggest that the hydrothermal method (for Ti catalyst) facilitated the crystal growth during material preparation. In the impregnation method (for 4Ti3Cu and 3Ti3Cu), the metals are distributed over the lower layer of the support of the catalyst; this causes the intensity of the peak to decrease compared to that prepared by the single component (Ti) hydrothermal method.

In this work, the TEM technique was employed to identify the position of the particles, size and morphologic features in the 3Ti3Cu nano-

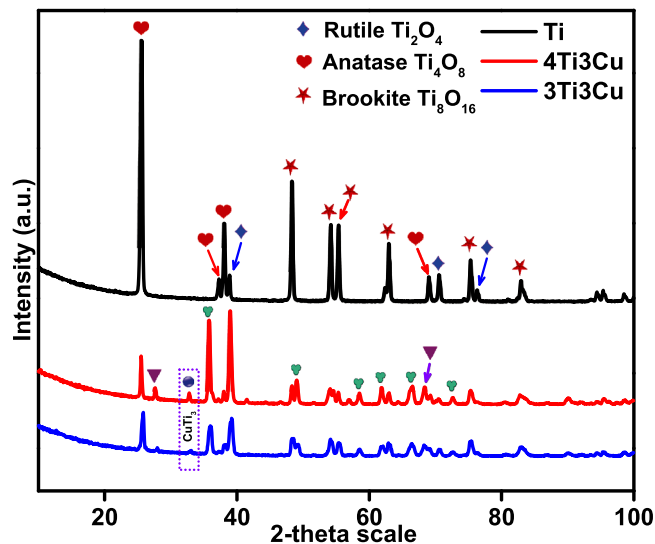


Fig. 3. XRD pattern for the Ti-Cu nano-catalysts.

catalyst; corresponding results are shown in Fig. 4. The nano-sized catalysts constituted a rectangular-like shape of TiO_2 with an average diameter of ~ 200 nm, indicating that the TiO_2 core is highly crystallized with better dispersion. However, Cu presented an uneven element form with less particle scattering. It also comprises segregated particles and appears in spherical shapes in mostly amorphous phases that are in good agreement with XRD results. This finding might be because of the less BET surface area and XRD crystal size of 3Ti3Cu compared with Ti catalyst, which was reported in previous sections. Less crystal size plays a substantial part in minimizing the coke production and deposition and enhancing the catalyst lifetime throughout the in-situ pyrolysis-catalytic steam reforming reaction process. Furthermore, as shown from the TEM micrograph, the contact between Ti and Cu particles was lower than those Ti particles. This suggests that Ti-Cu ensembles may be formed due to the interaction between Ti and Cu. And it is also confirmed that the highly dispersed nano-catalysts could be obtained with inexpensive materials via this simple hydrothermal-impregnation method.

As shown in Fig. 5, the FTIR spectrum utilizing the KBr pellet approach was obtained in the wavenumber range of 4000 – 400 cm^{-1} to analyze the practical clusters in the manufactured catalysts. The phenyl ring vibrations, such as $\gamma(\text{C}-\text{C}-\text{C})$, are identified at 1265 cm^{-1} [42]. This peak was shifted to 1203 cm^{-1} after introducing a CuO component to the TiO_2 . Giuseppe et al. [43] mentioned that the 1265 cm^{-1} peak could be assigned to the C-O vibration in guaiacyl rings that clearly shifted to a pronounced broad and strong band around 1203 cm^{-1} for the 4Ti3Cu and 3Ti3Cu catalysts due to the bending vibrations of amino acids side chains [44] and attributed to the asymmetric stretching vibrations of C-O-C in all samples [45]. A weak peak corresponding to $\text{C}=\text{O}$ is observed at 617 cm^{-1} for the bare Ti catalyst that can be assigned to $\omega\text{O}_1\text{-Ti}_3\text{-O}_2$ [46]. After introducing the Cu, the intensity of this peak is slightly increased and matches the metal oxide stretching, i.e., Cu-O bond in the monoclinic phase, which specifies CuO nanoparticles formation [47]. The band at 1018 cm^{-1} (symmetric O-C-O stretching [48]) belongs to the C-H and N-H in-plane deformation vibrations [49], and might also attribute to alkoxy groups attached to titanium ions in the catalysts [50]. FTIR bands at 1689 cm^{-1} are attributed to C=N vibrations modes [51]. Likewise, this band could also correspond to the $\nu(\text{C}-\text{O})$ mode of a carbonyl compound formed after adsorption [52].

H_2 -TPR characterization was implemented on all calcined samples to study the effects of adding Cu to Ti on the catalyst reducibility and the interaction between metal and support. It had been reported that the TPR profiles of Ti-based catalysts were affected by the interaction

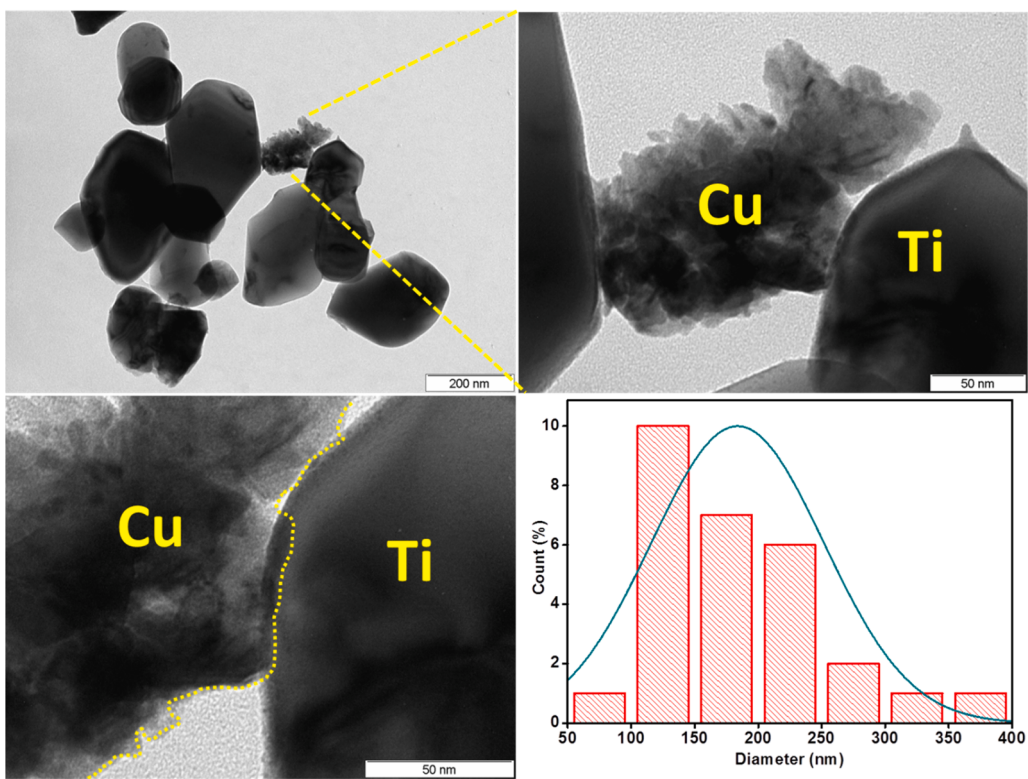


Fig. 4. TEM photos of the 3Ti3Cu nano-catalyst alongside its equivalent size delivery histograms.

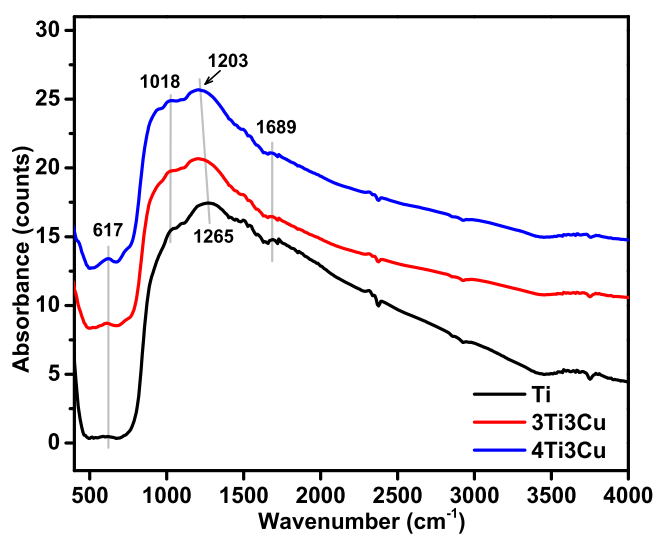


Fig. 5. Fourier-transform infrared spectroscopy-potassium bromide (FTIR-KBr) profiles of the fresh nano-sized catalysts.

between Ti and Cu. The reduction profiles of all catalysts are shown in Fig. 6(a), and the H₂ consumption are listed in Table 1. The less H₂ consumption corresponds to the poor reducibility of the catalyst. Compared to 4Ti3Cu and 3Ti3Cu samples, only a small trace of H₂ uptake in the Ti sample was detected, which might be associated with the reduction of the remaining TiO_x species in deficient concentration. The fact that the mixed metal oxides had solidified into a solution and the synergistic effects had boosted the reducibility is another potential explanation for the absence of pure Ti's reduction peaks. The observation of the low-temperature shoulders (281 °C and 315 °C), detected in reduction profiles of 4Ti3Cu and 3Ti3Cu, is possibly ascribed to the reduction of Cu²⁺ to Cu⁰ in aggregated copper oxide species. These

characteristics specify a highly distributed Cu²⁺ species in 4Ti3Cu and 3Ti3Cu catalysts, and the presence of these species can assign to the strong interaction among Cu and Ti. The two reduction peaks at 443 °C and 447 °C could be the reduction of monomeric Cu⁺ to Cu⁰ [53,54]. As a result, the species are reduced at much greater temperatures than Cu²⁺ species, which are associated with titanium copper alloy. As a result, we may conclude that the impregnated catalyst mainly comprises the copper oxides copper oxide and Cu-Ti. Due to the limited quantity of alloy or the high metal dispersion on the support, the Cu-Ti alloy peak is very weakly visible in the XRD examination. As presented in the figure, two main reduction peaks of the 4Ti3Cu catalyst were detected at about 443 °C, and 545 °C, which might be attributed to the reduction of surface oxygen and bulk oxygen of Cu, respectively, or may account for two overlapping reductions steps of copper oxide into Cu⁰. Noticeably, compared with the 3Ti3Cu catalyst, the reduction peaks of the 4Ti3Cu catalyst obviously shifted to a lower-temperature direction. These results reveal that the Ti species over 3Ti3Cu and 4Ti3Cu catalysts are more reducible, indicating that the reducibility of catalysts is promoted with higher Ti content. The lower the peak temperature, the better the reduction performance of the catalyst is. However, the peak area of the 3Ti3Cu catalyst was the largest, which can be concluded that the introduction of the Cu component promotes the reduction of the 3Ti3Cu catalyst, has the best redox capacity, largest H₂ consumption, oxygen storage capacity and inexplicable interactions among Ti and Cu as proven by the reduction peak at 600 °C.

The CO₂-TPD technique was employed to rationalize surface basicity and investigate basic sites' strength and distribution. The basicity curve is shown in Fig. 6(b). The quantitative analysis of surface-adsorbed CO₂ was conducted using the total peak area under the curves, and the findings are reported in Table 1. Nuanced surface characterization of porous materials is made possible by the adsorption of probe molecules, and molecules with certain characteristics (such as basic or acidic) can interact with the surface active sites that are inside the pores or between the layers. Therefore, we further characterized the basic sites by using pyrrole as a probe molecule in the DTG curve (Fig. 6(c)) and FTIR-KBr

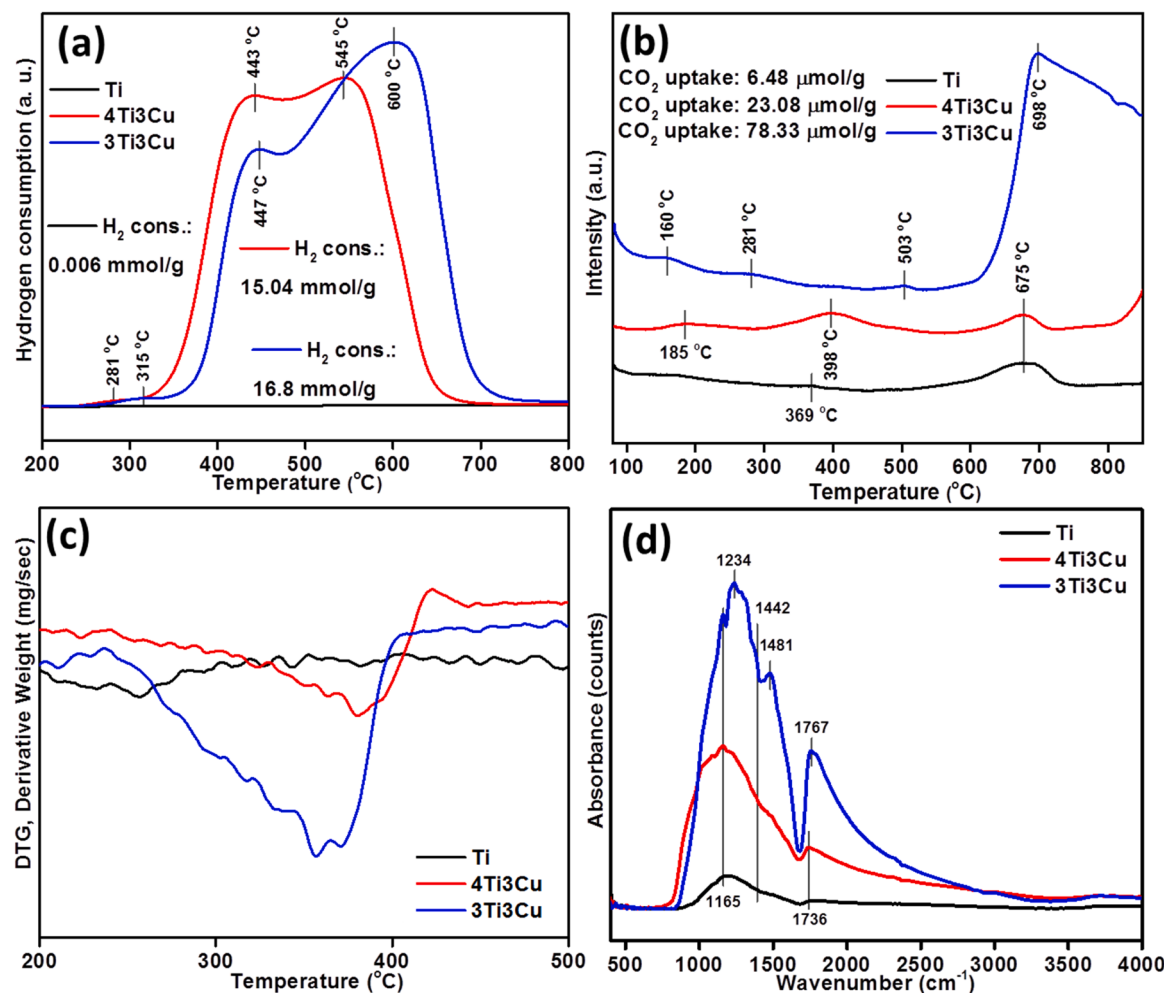


Fig. 6. (a) H₂-TPR curves, (b) CO₂-TPD curves, (c) pyrrole-Differential thermogravimetric analysis (DTG) curves, and (d) Pyrrole-FTIR spectra for the fresh Ti-Cu nano-catalysts.

curve (Fig. 6(d)). The proportion of basic sites may be used to gauge the total basicity, leading to the following pattern: 3Ti3Cu > 4Ti3Cu > Ti. This trend proves that the pure Ti had the weakest desorption peaks of CO₂, indicating its basicity was very weak and more basic sites are in the sample with higher Cu containing, while the basic strength of the sites is nearly the same. As shown in Fig. 6(b), the CO₂-TPD curves can be separated into three sorts of peaks equivalent to weak (50–250 °C), moderate (250–600 °C) and strong (>600 °C) basic phases for the catalysts. By moving the basic site peaks from 675 °C to the stronger area at 698 °C, the addition of Cu²⁺ to TiO₂ not only increases the value of overall basicity but also alters the distribution of basic sites. Catalysts with higher Ti concentrations (Ti and 4Ti3Cu) occupied strong basic strength within the weak, medium, and strong areas. However, the 3Ti3Cu catalyst had almost the same peaks at weak and medium regions, but one big intensity in the high-temperature range after 600 °C. This finding implies that because of the fundamental properties of the catalysts, the impregnation of Cu and Ti may promote additional surface sites for CO₂ adsorption.

The Pyrrole-DTG profile (Fig. 6(c)) illustrated that the peak intensities observed at the 200–500 °C region match the trend of CO₂-TPD and Pyrrole-FTIR spectra (3Ti3Cu > 4Ti3Cu > Ti). Pyrrole forms an adsorption layer on the Brønsted sites via the cycle's two subsequent carbon atoms, and these layers have substantially lower adsorption energies than Lewis sites. Pyrrole is an amphoteric molecule that may function as a proton acceptor through its π electron orbital or a proton donor to interact with basic sites on the surface. Surface basic sites

interacting with pyrrole are caused by the stretching and bending vibrational modes of surface formate (both –CH and –COO) and carbonate species over CuO and TiO₂ constituents, according to the Pyrrole-FTIR spectra. Bands at 1165 cm⁻¹, 1481 cm⁻¹, and 1736 cm⁻¹ were attributable to the C–CO–C stretch and bending, absorption of the phenyl ring, and C=O groups in amorphous Cu, respectively. There is a small shoulder at 1442 cm⁻¹, which can be proven that the Cu cause to increase in the Lewis basicity of the catalysts. This observation could explain that the increase in the basicity determined by CO₂-TPD with higher Cu charges is attached to the higher contribution of Lewis basic sites. The prevailing consensus is that Lewis basic sites correspond to oxygen anions with poor coordination formed as basic sites following the calcination stage. The coordination of the Lewis sites linked to O²⁻ anions determines their basicity. The oxygen atoms in the crystal corners have to be more basic than the oxygen atoms on the crystal faces or the edges [55]. The samples with smaller "crystal sizes" (as displayed in Table 1) should consequently have larger concentrations of Lewis sites with a low coordination number, and as a result, the basicity should be higher. Both Lewis acidic sites and Brønsted acidic sites may interact with pyrrole, as shown by the adsorption of this molecule on catalysts in its H⁺ form and on components in its alkali cation form, however, only the framework oxygen atoms can connect with this molecule at basic sites [56]. Hence, we further studied the Pyridine-FTIR and Pyridine-DTG for the acidity analysis.

However, it is noteworthy that Brønsted and Lewis's acid sites detected upon Pyridine-FTIR spectra and Pyridine-DTG curves exhibited

low acidity compared to Ti profile, probably due to the acidic $-\text{OH}$ on the catalyst surface. It can be seen that the band at 1542 cm^{-1} for the Ti profile (Fig. 7(a)) verified the existence of weak Brønsted acidic sites by developing pyridinium ions which also proved the existence of surface hydroxyl clusters [57]. Meanwhile, the incorporation of Cu on the Ti by impregnation technique increases the number of basic sites, weakening the acid possessions of 3Ti3Cu and 4Ti3Cu catalysts (Fig. 7(a) and (b)). The impregnation procedure resulted in the insertion of the Cu into the Ti structure and the creation of tiny Cu particles, which affects the number of acid sites due to the contact interface with other oxides, according to XRD data (Fig. 3). This weak Brønsted acidity hinges on the character of Cu phase species and influences plastic cracking reactions, including C–N bond cleavage. Another possibility is that the collapse of Cu's layered structure decreased the total acidity, which originated from the interlayer protons [58]. Thus, it is anticipated that the basic molecule's characteristics, the type of edge, and Ti's presence would affect how the proton transfers.

3.2. Catalytic performance

In a fixed-bed reactor setup, all of the reforming tests were conducted. Compared to other methods for producing H_2 fuel, in-situ pyrolysis-catalytic steam reforming is more complicated, primarily due to many coke precursors and carbon in plastic and phenol. All catalysts were first applied to a continuous reaction. The conversions of phenol and the production of H_2 , CO and CO_2 (in yield and mole percent) are shown in Fig. 8. The properties of the pyrolysis products for the 3Ti3Cu catalyst are listed in Fig. S2. Based on these observations, the conversion of phenol could be attributed to the transformation of the phenol molecule into H_2 formation via steam reforming reaction (Eq. 5). Low reforming performance was achieved under catalyst-free conditions (not shown). The H_2 yield and mole percent of pyrolysis-catalytic steam reforming after adding the bare Ti catalyst was 56.8% and 68.4%, respectively. H_2 production of the 4Ti3Cu catalyst was higher than the Ti sample, indicating that the Cu component played a key role in pyrolysis-catalytic steam reforming for H_2 production. At the same time, by associating the catalytic performance of Ti, 4Ti3Cu , and 3Ti3Cu , it can be found that the phenol conversion for the bare Ti catalyst was 84.9%, which was lower than those of Cu-added catalysts. The reason behind this might be due to the detection of Ti–Cu alloy as shown in the XRD analysis. Ashish and Qiang [59] mentioned that the bimetallic alloys cause higher catalytic effectiveness than their monometallic complements, owing to strong interaction among the metals. Therefore, for the 4Ti3Cu catalyst, the phenol conversions increased significantly compared to the pure Ti. Meanwhile, 3Ti3Cu showed the highest phenol

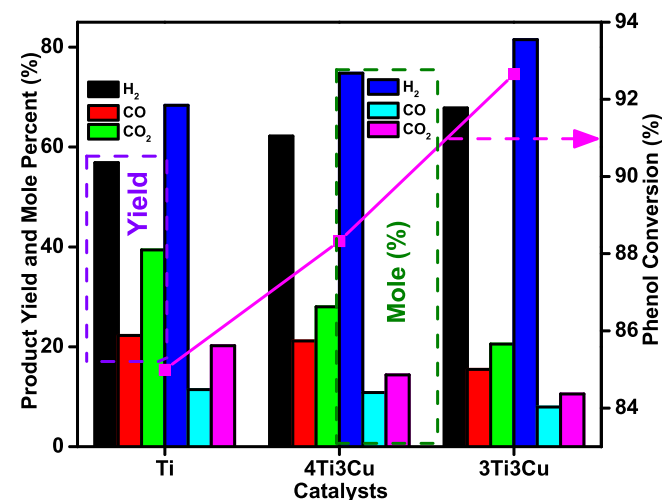


Fig. 8. The distribution of gas products in yield and mole % and phenol conversion for Ti, 4Ti3Cu and 3Ti3Cu nano-catalysts. Reaction conditions: (catalyst: 0.2 g, pressure: 1 atm, reaction temperature: 500°C , feed (PSW-phenol mixture) to water volume ratio of 1:9).

conversion (92.6%) and H_2 yield (67.8%), indicating that higher Cu loading has a catalytic activity in the in-situ pyrolysis-catalytic steam reforming process. This heightened activity of reducible 3Ti3Cu catalyst could be because of the strong metal-support interaction, higher reducibility, strong basicity and higher amount of sites analyzed by H_2 -TPR and CO_2 -TPD, respectively. Additionally, the phenol conversion result indicates that the 3Ti3Cu catalyst with a smaller crystallite size quickly adsorbs and activates phenol molecules compared to the catalyst with a large crystallite size. It means that catalysts with large crystallite sizes (as shown in Table 1 from XRD analysis) are not preferred because they cause higher coke formation [60,61] and cause catalyst deactivation. The higher basic site results in increasing the reaction rate [62]. The results as mentioned above suggest that the strong basic sites should be catalytically active sites in this base-catalytic reaction. When Cu was added to the catalyst, more surface basic sites were created, which improved CO_2 adsorption and carbonate synthesis. The carbonate was then hydrogenated by H_2 that was adsorbed on and activated by the Ti metallic sites. Strong basic sites created by the introduction of Cu species activated the hydroxyl group in phenol, increasing phenol conversion and H_2 selectivity. In the H_2 -TPR, the Cu^{2+} site was formed in the 3Ti3Cu catalyst due to the reducible characteristics of the Cu material. This resulted in a strong electron-donating property, a typical strong

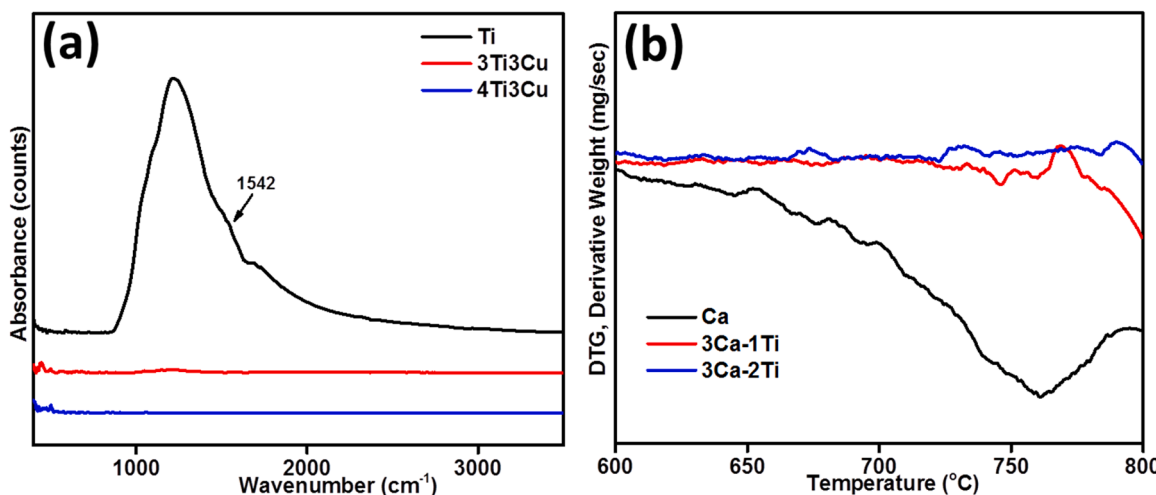


Fig. 7. (a) Pyridine-FTIR spectra and (b) Pyridine-DTG curves of the fresh catalysts.

metal support interaction effect that was beneficial to the catalytic activity. Previous research [63,64] stated that strong metal support interaction effect in good decoration of metal on the support, which is favourable in catalytic performance. Since basicity was shown to grow throughout the 3Ti3Cu sample, it can be inferred from the data above that basicity and activity are directly related. In fact, significant basicity that correlated with the most active catalyst was detected at high Cu concentrations. Therefore, Cu addition modifies the catalyst's acid function, which is primarily responsible for the carbon production, and positively impacts activity and catalytic stability by preventing carbon deposition on the catalyst's surface. Fig. 14 displays the results of a TGA study of the utilized catalysts, further supporting this claim. We performed the influence of temperature and time on stream tests, as shown in Fig. 9 and Fig. 10, believing that the increase in stability is predicted given the combination of the chemical and physical features of the 3Ti3Cu nano-catalyst.

The effects of reaction temperature on the catalytic performance of 3Ti3Cu are shown in Fig. 9. The H₂, CO and CO₂ yields, mole percent and phenol conversions were obtained after a 6 h evaluation for each temperature (6 runs and each run around 1 h) as a function of temperature. The slightly reverse water gas shift reaction (Eq. 7: CO₂ + H₂ → CO + H₂O) was promoted by increasing the temperatures. The situation that CO contents after reforming also increased with increasing temperatures could be related to the slight promotion of endothermic reactions. However, CO and CO₂ yield generally does not change appreciably compared to H₂ yield within the whole temperature range. The enhancement of phenol steam reforming reaction (Eq. 6: C₆H₅OH + 5 H₂O → 6CO + 8 H₂) by temperature can be observed as phenol conversion, and H₂ yield increased from 92.6% and 67.7% at 500 °C to 99.7% and 97.90% at 800 °C, respectively. This result suggests that the reaction process was dominated by phenol steam reforming reaction (PSR) (Eq. 6), which controls the final product distribution. Fig. 9 and Fig. 9 show that the reaction temperature of the 3Ti3Cu catalyst for the reforming of phenol may be reduced and that improved catalytic activity can be achieved, resulting in a decrease in the cost of catalyst manufacturing. In light of this, it is clear that phenol steam catalytic reforming for the generation of H₂ is advantageous and that low-temperature catalytic reforming is feasible. Hence, this study confirms the feasibility of H₂ generation from the in-situ pyrolysis-catalytic steam reforming reaction of PSW dissolved in phenol at temperatures less than 600 °C, which is practically more sustainable and requires less energy.

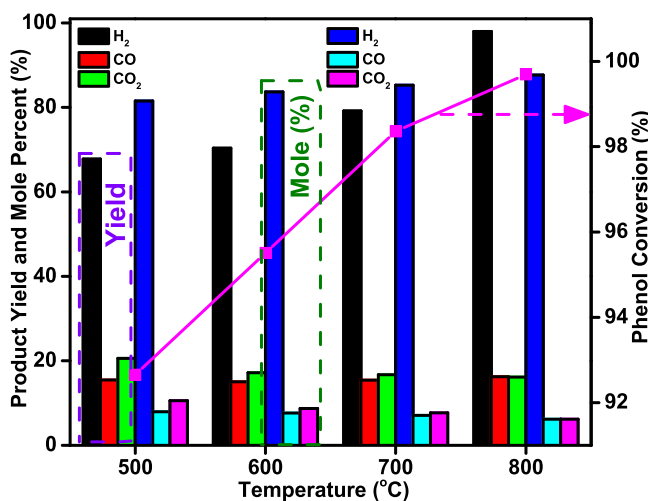


Fig. 9. The concentrations of gaseous products in yield and mole % and phenol conversion for the 3Ti3Cu nano-catalysts. Reaction conditions: (catalyst: 0.2 g, pressure: 1 atm, reaction temperature: 500 °C-800 °C, feed (PSW-phenol mixture) to water volume ratio of 1:9).

To further investigate the stability of the precious metal-free Ti-Cu nano-catalyst, the endurance experiments were conducted over the 3Ti3C catalyst at 500 °C for 45 h. The changes in phenol conversion and H₂ yields and mole percent as a function of time on stream during the in-situ pyrolysis-catalytic steam reforming reaction of PSW dissolved in phenol are shown in Fig. 10. The catalyst shows a highly stable behavior for all time ranges in terms of mole percentage. The yields of CO and CO₂ hardly changed over 3Ti3C, evidencing better stability. In contrast, H₂ yield and phenol conversion decreased from 67.8% and 92.7% at the first hour to 59% and 89.9% after 25 h time-on-stream. The rapid decrease of the conversion into the gas phase indicates the deactivation of the 3Ti3C catalyst; consequently, this pattern during a 25 run has prompted us to conduct a longer-term evaluation of the catalyst's resistance to the reaction. In spite of the severe reaction conditions and decrease in catalytic performance after 25 h of time-on-stream, an improvement can be observed at 30–45 h with a slightly decreased in H₂ yield and phenol conversion, which may be related to an occurrence of slight deactivation of catalysts by carbon deposits [65,66]. The article will go into more detail on how the deactivation of the catalyst is related to the deposition of coke, the sintering and aggregation of active metal particles, and other factors.

The main products analyzed from the prominent peaks in the GC/MS chromatogram are listed in Fig. S2. The chromatogram of GC-MS technique for the 3Ti3Cu nano-catalyst confirmed that three value-added components were produced upon the pyrolysis reaction of PSW-phenol. Nevertheless, the mass spectrometer's limitations prevent it from detecting low molecular weight gases. The catalytic pyrolysis products were classified into aromatic compounds such as ethylamine and oxygenated aromatics such as tert-butyl hydroperoxide and benzene, (1,1-dimethylethoxy) (BDE). Tert-butyl hydroperoxide (TBHP), an alkyl hydroperoxide with a tert-butyl group, was found to be the major liquid result of the pyrolysis process of PSW-phenol. It is frequently employed in several oxidation processes. It functions as an oxidizing agent and an antibacterial agent. For example, to produce chain-elongated peroxides, Chuan et al. [67] described a practical Fe-catalyzed decarbonylative alkylation-peroxidation of alkenes using aliphatic aldehydes and TBHP. To produce α -ketoamides, Xiaobin and Lei [68] described a brand-new and effective TBHP/I₂-promoted oxidative coupling process of acetophenones with amines. Therefore, in addition to a small amount of BDE, value-added components such as TBHP can also be found in the pyrolysis liquid product of PSW dissolved in phenol. The pyrolytic products were further analyzed by FTIR analysis, and the results are shown in Fig. 11.

The produced liquid component from the in-situ pyrolysis-catalytic steam reforming reaction of PSW dissolved in phenol using 3Ti3Cu nano-catalysts was also straight analyzed by FTIR to categorize the dominating functional clusters, and the results are shown in Fig. 11. FTIR can be used to analyze the chemical composition and the optical properties of the material and to better understand the release characteristics of liquid products after the reaction. All samples showed a broad band spectrum at 401, 424, 447, 864, 1049, 1165, 1296, 1620, and 2955 cm⁻¹ wavenumber and FTIR results with the peak intensities are shown in Fig. 13. Below 3000 cm⁻¹, one band is detected at 2955 cm⁻¹, which is attributed to aliphatic vibrations $-\text{CH}_2-$ [69,70]. The absorption bands at 1620 cm⁻¹ correspond to the C=C stretching mode of carbonyls and indicate the presence of compounds containing aromatic rings [71,72] and benzene (C=C) in specific [73]. Also, aliphatic C-O stretching was observed at 1296 cm⁻¹ [74]. This peak is also ascribed to the detection of the aldehydes, alkanes, and ethers [75]. The band at 1165 cm⁻¹ was assigned to the stretching vibration of C-O-C [76]. In accordance with the previous research [77], C-H stretch in methyl, methylene, and methyne groups can be confirmed at the spectral range around the band at 1049 cm⁻¹. Rainer et al. [78] stated that this peak could also be assigned to the C-O-C symmetric stretching in aliphatic groups and acid derivatives. In addition, there were four autocorrelated peaks at 864, 447, 424, and 401 cm⁻¹ that confirmed the formation of

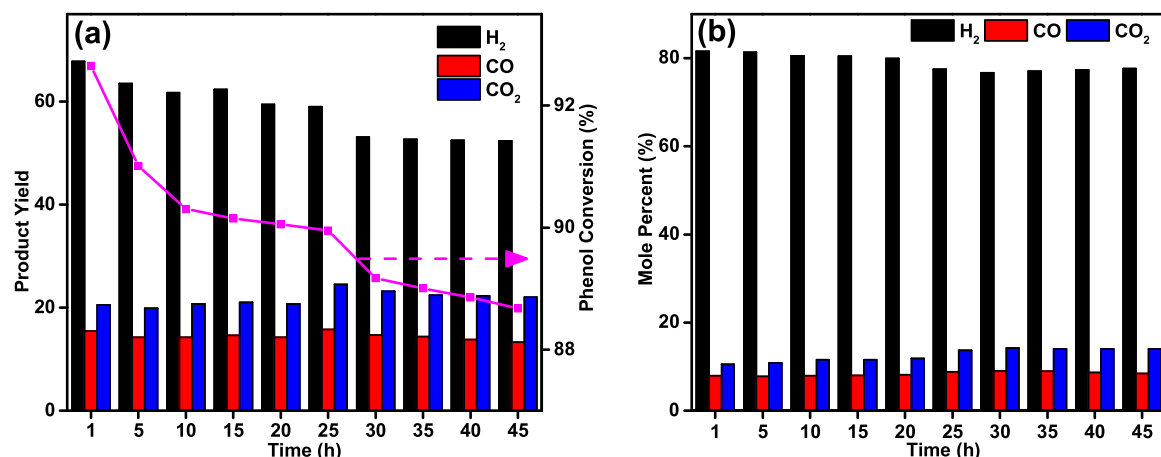


Fig. 10. Time-on-stream stability results for 3Ti3Cu nano-catalyst at 500 °C based on (a) product yield and phenol conversion and (b) product mole percent.

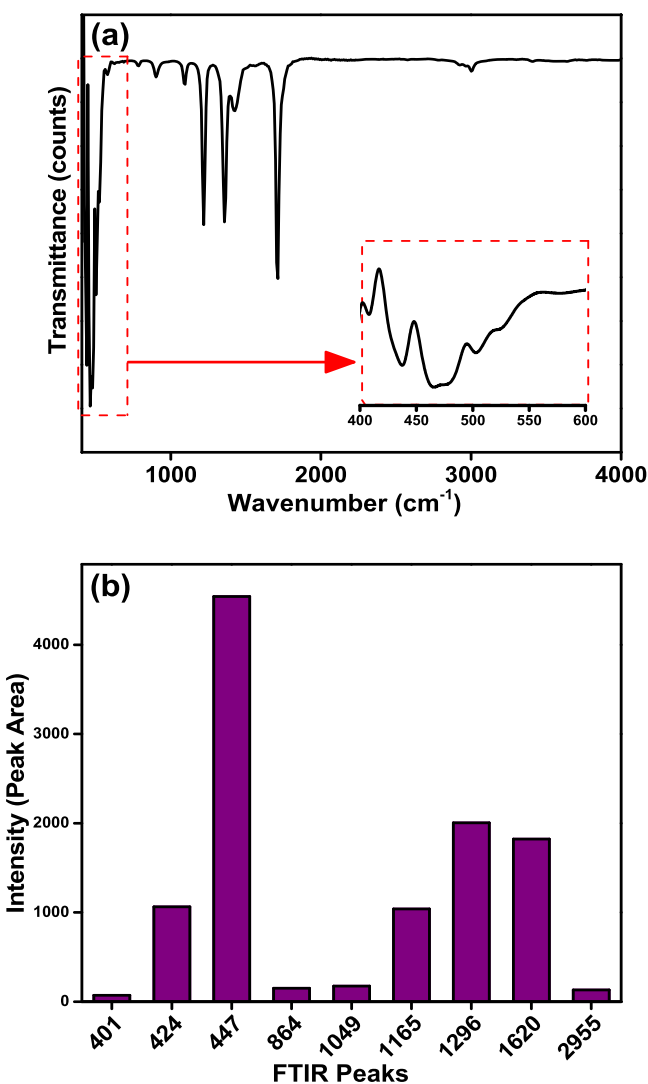


Fig. 11. FTIR bands of the pyrolysis liquid product along with the summary of band strengths based on peak areas.

out-of-plane C–H bending vibration peak for the aromatic ring [79], ν CN stretching band (ν C≡N) [80], τ Ring (ring torsion) and γ CN (out-of-plane bending or wagging) [81], and deformation modes [82] (which is connected with torsions and bending of benzene ring [83]), respectively.

The C–C group is hardly ever present throughout the pyrolysis process, indicating that the C–C break is exceedingly challenging. Heating rates can impact the C=O and C–H groups.

3.3. Characterization of the used catalysts

Several characterizations, including BET surface area, N₂ adsorption–desorption isotherms and pore size distribution, TGA, DTG, CHNS, and TEM, were performed to investigate the deposited carbon and metal sintering over the used catalysts. An evaluation of the textural characteristics of fresh and spent catalysts (surface areas, pore volume, and average pore size) is presented in Table 2. N₂ adsorption–desorption isotherms and pore size distribution of spent catalysts are also illustrated in Fig. 12. The monolayer-multilayer adsorption on the material's interior surfaces is responsible for the initial portion of the curve (at low P/P⁰). It is possible to explain the sharp rise in isotherm slope for high P/P⁰ over 0.90 by capillary condensation inside the pores, followed by saturation when the pores get saturated with liquid [84,85]. All the spent catalysts present almost the same Type-IV isotherm and an H₁ hysteresis loop to the Ti and 4Ti3Cu and double-hysteresis loops for the 3Ti3Cu. This means the mesoporous nature of the catalysts after the reaction is maintained, and the reactions did not substantially impact the main pore structures of the catalysts. The pore size distribution for spent Ti and 4Ti3Cu catalysts was positioned in the region of 5–15 nm, while it was 17–35 nm for the 3Ti3Cu catalyst. The decrease in specific surface area of Ti is large (> 70%) with the smallest diameter pores (20 nm), which indicated the surface and pores of the Ti catalyst were blocked with ashes, carbon, residues or poison reactants. The weakened surface area of the Ti catalyst in comparison with the fresh catalyst might also be because of the collapsing of microchannels in the catalyst structure by the collision of energetic particles during the reaction procedure [86,87]. The surface area and total pore volume of the 4Ti3Cu and 3Ti3Cu catalysts increased after the reaction; probably, an acidic treatment by phenol compound occurred during the reaction, which resulted in the removal of blockage metal on pores. This opens up the pores in the used catalyst that were closed by dangerous metals, increasing the specific surface area of the used catalyst in comparison to the new catalyst. This would increase the access of reactant molecules to the active site of the catalyst within the pores and increase the activity. The better performance of the 3Ti3Cu catalyst could be due to their enhanced basicity strength and the stable catalytic performance compared to the Ti, and 4Ti3Cu catalysts could be attributed to their structural stability during the reforming reaction.

One of the traditional techniques in FTIR spectroscopy has been around from the beginning and includes pressing or grinding a tiny quantity of a dry solid sample with powdered IR-transparent substances

Table 2

Weight loss, surface area, and carbon contents of the spent nano-sized catalysts.

Catalysts	Weight loss (%) WL ₁	WL ₂	WL ₃	Total weight loss (%)	Fresh catalyst Surface area (m ² /g)	Spent catalyst Surface area (m ² /g)	Pore-volume (cm ³ .g ⁻¹)	Pore-diameter (nm)	Carbon Content (wt%) ^a
Ti	63.3	0.0	0.0	56.2	15.912	10.206	0.0517	20.26	8.2
4Ti3Cu	7.6	10.2	26.9	44.7	5.374	8.450	0.0462	21.87	2.1
3Ti3Cu	6.6	0.0	0.0	0.0	3.730	22.748	0.1727	30.37	0.0

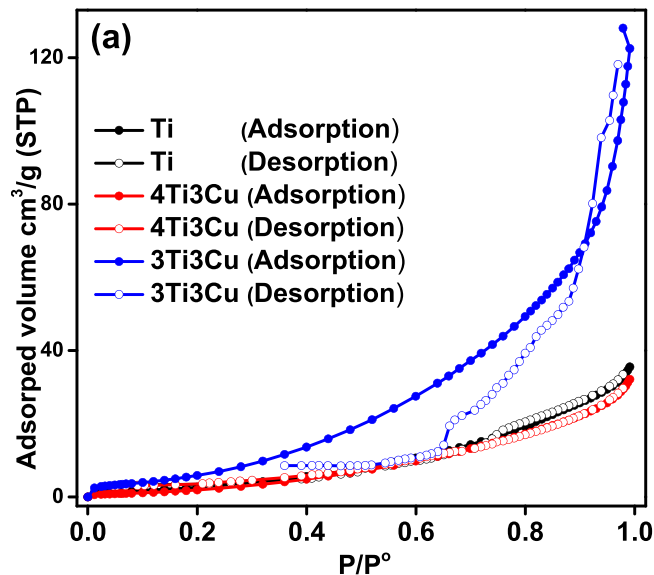
^aCarbon wt% was determined by CHNS elemental analysis

Fig. 12. (a) N₂ adsorption and desorption isotherms and (b) pore size distribution of the used catalysts.

like halide salts, with KBr being the most popular [88]. Fig. 13 shows the outcomes of using FTIR as a surface analysis approach to detect functional groups in the used catalyst, focusing on unsaturated hydrocarbons (C=C linkages) and aromatics. All samples of spent catalyst were pelletized with KBr following the same procedure described in Section 2.2. The FTIR peak of the spent catalysts in 3757 cm⁻¹ fits to the surface-linked hydroxyl groups; this peak is steadily enhanced with higher Cu content, proving the catalysts have been regenerated. Also, the samples present a slender but distinct vibration near 2376 cm⁻¹,

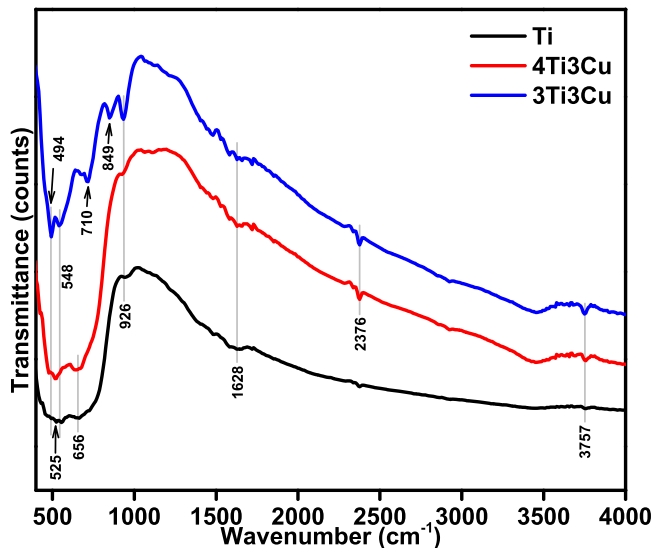


Fig. 13. FTIR-KBr profiles of the spent nano-sized catalysts.

which is characteristic of the ν_3 elongation mode of linearly adsorbed CO₂ on Cu²⁺. This peak can also be assigned to stretching vibrations of the reactants' secondary $\text{--N}=\text{H}$ groups [89]. Due to the C=O stretching of the carboxyl groups, the spent catalysts displayed distinct bands at 1628 cm⁻¹. As the intensities increase, more carboxyl groups are produced. The fact that this peak has a higher intensity indicates that Cu⁺'s incorporation causes the creation of basic sites, which is compatible with its amphoteric capabilities. These bands could be related to species of H₂ carbonates created when CO₂ interacts with hydroxyl groups. A very weak sharp absorbance peak at 926 cm⁻¹ could be ascribed to the asymmetric stretching vibrations of Ti-O-Ti bonds that increased in intensity by additional Cu. The absorbance peaks placed at 548 cm⁻¹ and 494 cm⁻¹ corresponded to the TiO₂ lattice and signified the presence of functional groups like metals [90] and related to symmetric stretching vibrational modes [91], respectively. The 548 cm⁻¹ band might also be associated with O-Ti-O and Ti-O-Ti modes overlapping with O-Cu and Cu-O-Ti bonds because it has high intensities for the spent 3Ti3Cu and 4Ti3Cu catalysts. The two absorbance peaks at 525 and 656 cm⁻¹ for the bare Ti and 4Ti3Cu spent catalysts correspond to the bending of Ti-O vibrations (and could also be related to the detection of V=O bonds [92]) and the bending of -OH in the -C-OH group [93], respectively. In the 3Ti3Cu spent sample, two strong absorption peaks at 849 cm⁻¹ (probably related to the vibrations of the aromatic cycle [94]) and 710 cm⁻¹ (can be ascribed to rocking modes of $-(\text{CH}_2)_n-$ alkyl chains with $n \geq 4$ [95]) were detected which have not appeared for the Ti and 4Ti3Cu catalysts. The bands at 849 cm⁻¹ are involved in Ti=O stretching vibrations of orthorhombic Ti₈O₁₆ and could also represent the symmetric Ti-O stretching ν_1 . The band at 710 cm⁻¹ might also be originated from in-plane bending of the CO₃²⁻ group [96].

Large organic compounds that contain C-H or C-C bonds might be trapped in the cages of acidic catalysts, which invariably results in catalyst deactivation under reaction circumstances. The in-situ

pyrolysis-catalytic steam reforming process generates large organic compounds. Therefore, one crucial economic goal for the industrial use of these catalysts is to comprehend coke production. Herein, we analyzed the coke formation after reaction by TGA, DTG and CHNS techniques. Thermogravimetric analysis (TGA) is a thermal analytical technique extensively used to understand and measure the amount of coke deposited on the catalyst after the reaction. DTG gives information about the rate at which these coke are removed concerning time or temperature. The elemental analyzer (CHNS) is a technique used for quantitative determination in organic samples containing carbon and other basic elements of nature. The TGA and DTG curves of the spent catalysts are shown in Fig. 14, and quantitative weight loss data (taken from TGA and CHNS) is shown in Table 2. The weight loss processes could be separated into three phases and mentioned by weight loss (WL). The vaporization of moisture caused the first phase below about 200 °C, the second phase (WL₂) between 200 and 600 °C was attributed to the burning of deposited coke, and the third phase (WL₃) above about 600 °C belonged to the decomposition of remaining residues and heavy carbonaceous species. The in-situ pyrolysis-catalytic steam reforming reaction of PSW-phenol over Ti catalyst formed the highest amount of coke (8.2 wt%) with 56.2% of the total weight loss. The most significant mass drop for the Ti spent sample was at 77 °C, caused by the release of phenol and water molecules. The coke analysis results obtained for the

Ti catalyst revealed that there is a significant interaction between Ti catalyst pore structure (pore size and shape) (as analyzed by pore size distribution in Fig. 2(b), XRD crystallinity in Fig. 3 and Table 1). The intensity of acid sites (Fig. 8) greatly affects Ti coke formation and deposition in converting PSW-phenol to H₂. In the first stage, the weight loss for the 4Ti3Cu and 3Ti3Cu took place at the temperature of 91.7 °C and was 7.6% and 6.6%, respectively. The DTG curve of the 4Ti3Cu catalyst showed a broad peak at 752 °C, which was associated with light and heavy composites inside the 4Ti3Cu catalyst. The pyrolysis of phenol and the production of tiny derivatives from the fracture of PSW should yield light chemicals. Nevertheless, the bio-oil derivatives or the big aromatics made from the PSW structure were given credit for the heavier compounds. In both WL₂ and WL₃ phases, there was no coke development on the surface of the TGA curves of the Ti and 3Ti3Cu samples. The weight rise in this catalyst profile may have been caused by the oxidation of the metallic, active sites [10,23]. The DTG curve of the 3Ti3Cu sample shows almost straight like in all stages, indicating that the sample was stable in the entire temperature range. The lack of mass loss percentage in the experiment with 3Ti3Cu can be due to its low BET surface area (see Table 1) and slit-shaped pores structure. The slit-shaped pores structure has an advantage in contribution to the diffusion of oxygen during coke combustion [97]. This is perhaps due to the fact that the high content of Cu increases the basic site on the catalyst surface too much, which is not conducive to the phenol reforming reaction. The lowest weight loss for the 3Ti3Cu might also be due to the strongest metal-support interaction and strongest basic sites. The carbon content of the spent catalyst also follows the catalyst reducibility and basicity (Fig. 6) characterizations. The lowest carbon content has been taken place for the catalyst with the highest H₂ consumption and CO₂ uptake (Table 1). As a result of the intrinsic fundamental properties of 3Ti3Cu, which operate as a sponge for CO₂ absorption, local gradients in gas concentration are generated, which promotes improved process efficiency. In fact, relative to rates of cracking side reactions, basic sites are thought to produce substantially higher rates of products and reagents desorbing from the catalyst surface [98]. The aforementioned characteristics of 3Ti3Cu made it an optimum catalyst for the in-situ pyrolysis-catalytic steam reforming reaction of PSW dissolved in phenol.

Using the TEM method, we investigated the coke deposition over the employed catalysts in this study. The three forms of carbon that are deposited on the catalysts are amorphous ($T \leq 570$ °C), filamentous (570 °C < $T < 1000$ °C), and graphitic (≥ 1000 °C). At the lowest temperature range of T570°C, amorphous carbon is produced, then filamentous carbon at T570°C to T1000°C, and lastly, graphitic carbon at T1000°C [99]. The morphology results of the spent 3Ti3Cu catalyst are depicted in Fig. 15, which illustrates that the reaction produced carbon with random shapes and morphologies, but mainly filamentous carbon or carbon nanofibers (CNFs) on the catalyst surface were observed. The diameters of CNFs are in the range of 20–80 nm, and pores have widened due to the pores filling. The 3Ti3Cu catalyst exhibits a similar tubular shape and sphere-like geometry with particle sizes of 20–50 nm. The catalyst revealed the existence of Cu particles on the surface, which were corroborated by well-dispersed, small particle TEM images. In contrast, the grey forms on the surface are associated with TiO₂ components. The CNFs and filamentous coke did not block catalyst particles, although its progressive deposition may hinder the contact between reactants and catalyst active sites. Additionally, due to the strong Cu-Ti interaction, the Cu was not removed by the growing CNFs, and very low fragmented particles were observed. A catalyst may get fragmented during the in-situ pyrolysis-catalytic steam reforming reaction process as a result of internal catalyst reactions where carbons are first created and then developed. Smaller metal particle sizes likely helped to generate the thinner CNFs, and the thinner CNFs had greater surface energies, making them less stable. This makes it very simple to remove CNFs made with smaller Cu particles, which may be why the 3Ti3Cu catalyst exhibits the least carbon deposition in TGA. The figure clearly illustrates a nearly perfect core–shell morphology was obtained. The different shell

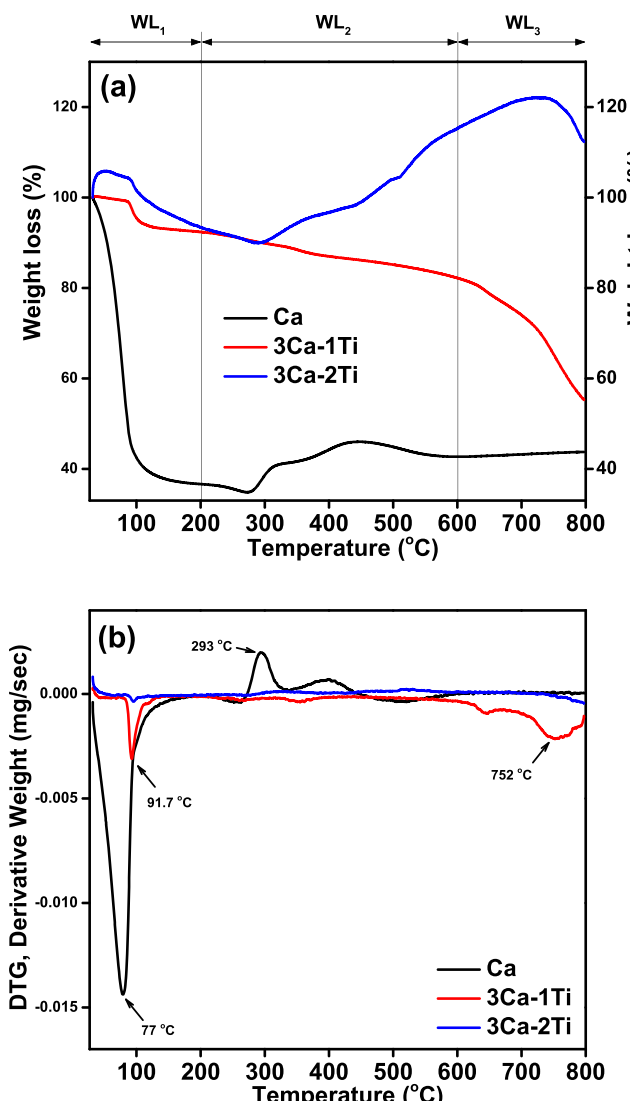


Fig. 14. (a) TGA and (b) DTG curves of used catalysts.

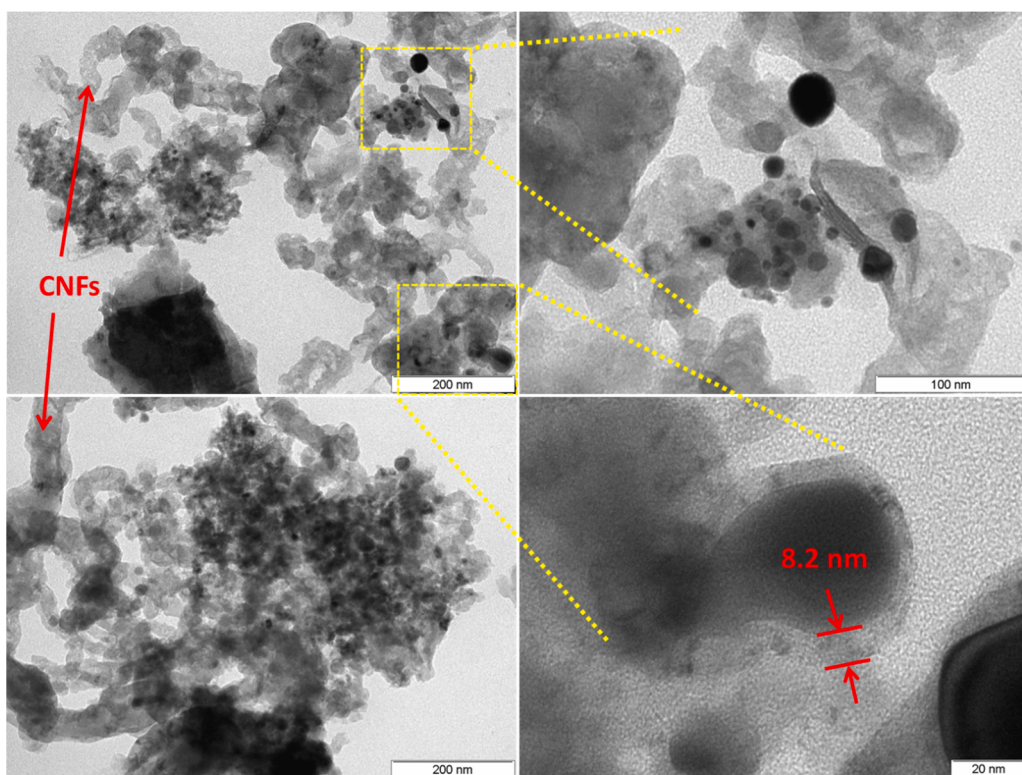


Fig. 15. TEM images of the used 4Ti3Cu nano-catalyst.

thicknesses with spherical cores with around 30 nm diameters result from the reaction. This reaction produced a core shell-like structure with an approximate shell thickness of 8.2 nm. The key benefits of core-shell nanoparticles are that the core material's qualities, such as reactivity, may be reduced, and its thermal stability can be altered, increasing the core particle's overall stability and dispersibility. The shell materials, which can provide surface chemistry for further modifying and functionalizing the nanoparticles, are another advantage of core-shell structures. In conclusion, the in-situ pyrolysis-catalytic steam reforming process of PSW dissolved in phenol may be sustained by catalysts with increased basicity, and the catalyst can prevent complex carbon deposition.

4. Conclusions

To summarize, nano-sized precious metal-free Ti-Cu catalysts were successfully synthesized by direct hydrothermal conditions and impregnation method and innovatively applied in the in-situ pyrolysis-catalytic steam reforming reaction of PSW liquefied in phenol. This study is expected to offer an essential research reference for designing precious metal-free Ti-Cu and producing H₂ and valuable liquid fuel from the abovementioned reaction. As-prepared samples were analyzed by XRD, BET, CO₂-TPD, pyrrole-DTG, pyrrole-FTIR, pyridine-FTIR, pyridine-DTG, TEM, H₂-TPR, FTIR-KBr and the used samples were characterized by TGA-DTG, FTIR-KBr, BET, TEM and CHNS. The liquid product was also analyzed by GC/MS and FTIR systems. The morphology study suggested that Ti-Cu ensembles may be formed due to the interaction between Ti and Cu that lead to the structure of CuTi₃ alloy, as confirmed by XRD analysis. Samples with higher Cu contents cause to decrease in the surface area, crystal sizes, partial collapse of ordered mesoporous structure and the growth of the average pore diameter. However, Cu results in higher reducibility, metal support interaction and basic sites of the catalysts with highly dispersed Cu²⁺ species in 4Ti3Cu and 3Ti3Cu samples. Cu²⁺ insertion into TiO₂ changes the distribution of basic sites as well as the total basicity value. The

3Ti3Cu performed the best catalysis performance, highest phenol conversion, H₂ production and lowest coke formation due to strong metal-support interaction, higher reducibility, strong basicity and higher amount of sites analyzed by H₂-TPR and CO₂-TPD, respectively. The H₂ selectivity rose, and the coke quantity dropped from 4Ti3Cu and 3Ti3Cu due to decreased acid sites and increased basic sites, providing increasingly continuous catalytic activity. The catalytic pyrolysis products were classified into aromatic compounds, such as ethylamine, and oxygenated aromatics, such as tert-butyl hydroperoxide and benzene, (1,1-dimethylethoxy). These results may help in the development of more effective solid base catalysts for a variety of base-catalyzed processes.

CRediT authorship contribution statement

W. Nabgan First author, contents development, writing. H. Alqaraghuli Experimental section. B. Nabgan Writing, editing. T.A. Tuan Abdullah Supervision, English editing. M. Ikram Writing (Section 2), editing. F. Medina Comments and editing. R. Djellabi Writing, Revision, response to reviewer, proofreading and English editing.

Declaration of Competing Interest

The authors declare that they have no known competing financial interests or personal relationships that could have appeared to influence the work reported in this paper.

Data availability

No data was used for the research described in the article.

Acknowledgments

The principal author, Walid Nabgan, is thankful for the support from Universitat Rovira i Virgili under the Maria Zambrano Programme

(Reference number: 2021URV-MZ-10), Proyectos de Generación de Conocimiento AEI/MCIN (PID2021-123665OB-I00), and the project reference number of TED2021-129343B-I00. The authors are also grateful for the support given by Universiti Teknologi Malaysia (UTM) allocation budget in Pusat Pengurusan Makmal Universiti (PPMU) laboratory.

Appendix A. Supporting information

Supplementary data associated with this article can be found in the online version at doi:10.1016/j.apcatb.2022.122279.

References

- [1] M. Gholizadeh, C. Li, S. Zhang, Y. Wang, S. Niu, Y. Li, X. Hu, Sustain. Energy Fuels 4 (2020) 5885–5915.
- [2] H. Zhou, A. Meng, Y. Long, Q. Li, Y. Zhang, Renew. Sustain. Energy Rev. 36 (2014) 107–122.
- [3] M. Ripa, G. Fiorentino, H. Giani, A. Clausen, S. Ulgiati, Appl. Energy 186 (2017) 211–225.
- [4] A. Fivga, I. Dimitriou, Energy 149 (2018) 865–874.
- [5] V. Dhyani, T. Bhaskar, Renew. Energy 129 (2018) 695–716.
- [6] K. Boyle, B. Örmeci, Water 12 (2020).
- [7] F.F. Annike, Z. Hafid, R.S. Pd, Study on solubility of plastic bottle waste in phenol solution, The 2nd International Seminar on Chemical Education 2017, 2017.
- [8] B. Nabgan, T.A.T. Abdullah, M. Tahir, W. Nabgan, I. Saeh, Y. Gambo, Malay J. Catal. 2 (2017) 18–22.
- [9] T. Abbas, M. Tahir, N.A. Saidina Amin, Ind. Eng. Chem. Res. 58 (2019) 517–530.
- [10] W. Nabgan, T. Tuan Abdullah, R. Mat, B. Nabgan, Y. Gambo, A. Johari, Appl. Sci. 6 (2016) 223.
- [11] S.D. Anuar Sharuddin, F. Abnisa, W.M.A. Wan Daud, M.K. Aroua, Energy Convers. Manag. 115 (2016) 308–326.
- [12] S. Budsareechai, A.J. Hunt, Y. Ngernyuen, RSC Adv. 9 (2019) 5844–5857.
- [13] B. Nabgan, M. Tahir, T.A.T. Abdullah, W. Nabgan, Y. Gambo, R. Mat, I. Saeh, Int. J. Hydrogen Energy 42 (2017) 10708–10721.
- [14] W. Nabgan, B. Nabgan, T.A. Tuan Abdullah, M. Ikram, A.H. Jadhav, A.A. Jalil, M. W. Ali, ACS Omega 7 (2022) 3324–3340.
- [15] M. Navlani-García, K. Mori, D. Salinas-Torres, Y. Kuwahara, H. Yamashita, Front. Mater. 6 (2019).
- [16] S. Fang, Y. Liu, Z. Sun, J. Lang, C. Bao, Y.H. Hu, Appl. Catal. B: Environ. 278 (2020), 119316.
- [17] X. Peng, Y. Mi, X. Liu, J. Sun, Y. Qiu, S. Zhang, X. Ke, X. Wang, J. Luo, J. Mater. Chem. A 10 (2022) 6134–6145.
- [18] A. Gamal, K. Eid, A.M. Abdullah, Int. J. Hydrogen Energy 47 (2022) 5901–5928.
- [19] P. Zhou, H. Chen, Y. Chao, Q. Zhang, W. Zhang, F. Lv, L. Gu, Q. Zhao, N. Wang, J. Wang, S. Guo, Nat. Commun. 12 (2021) 4412.
- [20] W. Nabgan, R. Mat, T.A.T. Abdullah, B. Nabgan, Y. Gambo, Z.Y. Zakaria, J. Environ. Chem. Eng. 4 (2016) 4444–4452.
- [21] W. Nabgan, T.A. Tuan Abdullah, R. Mat, B. Nabgan, U.A. Asli, A. Johari, J. Teknol. 78 (2016) 77–82.
- [22] W. Nabgan, T.A. Tuan Abdullah, R. Mat, B. Nabgan, Y. Gambo, K. Moghadamian, J. Environ. Chem. Eng. 4 (2016) 2765–2773.
- [23] W. Nabgan, T.A. Tuan Abdullah, R. Mat, B. Nabgan, Y. Gambo, S. Triwahyono, Int. J. Hydrogen Energy 41 (2016) 22922–22931.
- [24] W. Nabgan, T.A. Tuan Abdullah, R. Mat, B. Nabgan, S. Triwahyono, A. Ripin, Appl. Catal. A: Gen. 527 (2016) 161–170.
- [25] D.H. Kim, J.H. Kim, Y.S. Jang, J.C. Kim, Int. J. Hydrogen Energy 44 (2019) 9873–9882.
- [26] K.A. Trowell, S. Goroshin, D.L. Frost, J.M. Bergthorson, Sustain. Energy Fuels 4 (2020) 5628–5635.
- [27] A.A. Ibrahim, A.H. Fakeeha, A.S. Al-Fatesh, A.E. Abasaeed, W.U. Khan, Int. J. Hydrogen Energy 40 (2015) 7593–7600.
- [28] A.A. Ibrahim, A.S. Al-Fatesh, W.U. Khan, M.A. Soliman, R.L.A.L. Otaibi, A. H. Fakeeha, J. Chin. Chem. Soc. 62 (2015) 592–599.
- [29] S.I. Nikitenko, T. Chave, X.L. Goff, Part. Part. Syst. Charact. 35 (2018), 1800265.
- [30] Y. Wang, Z. Hong, D. Mei, Int. J. Hydrogen Energy 46 (2021) 6734–6744.
- [31] J.-H. Lee, E.-G. Lee, O.-S. Joo, K.-D. Jung, Appl. Catal. A: Gen. 269 (2004) 1–6.
- [32] Y. Liu, H. Kang, X. Hou, S. Qing, L. Zhang, Z. Gao, H. Xiang, Appl. Catal. B: Environ. (2022), 122043.
- [33] W. Nabgan, B. Nabgan, T.A.T. Abdullah, M. Ikram, A.H. Jadhav, M.W. Ali, A. A. Jalil, Catal. Today 400–401 (2022) 35–48.
- [34] B. Nabgan, W. Nabgan, T.A. Tuan Abdullah, M. Tahir, Y. Gambo, M. Ibrahim, W. Syie Luing, Energy Convers. Manag. 142 (2017) 127–142.
- [35] W. Nabgan, B. Nabgan, T.A. Tuan Abdullah, H. Alqaraghuli, N. Ngadi, A.A. Jalil, B. M. Othman, A.M. Ibrahim, T.J. Siang, Int. J. Hydrogen Energy 45 (2020) 22817–22832.
- [36] W. Nabgan, B. Nabgan, M. Ikram, A.H. Jadhav, M.W. Ali, A. Ul-Hamid, H. Nam, P. Lakshminarayana, K. Ankit, M.B. Bahari, N.F. Khusnun, Chemosphere 290 (2022), 133296.
- [37] W. Nabgan, B. Nabgan, T.A. Tuan Abdullah, A.A. Jalil, A. Ul-Hamid, M. Ikram, A. H. Nordin, A. Coelho, J. Anal. Appl. Pyrolysis 154 (2021), 105018.
- [38] J.H. Park, C. Park, K.S. Lee, S.J. Suh, AIP Adv. 10 (2020), 115220.
- [39] Z. Shao, Q. Shen, H. Ding, Y. Jiang, S. Li, G. Yang, Ceram. Int. 48 (2022) 11836–11848.
- [40] N.N.M. Ghani, A.A. Jalil, S. Triwahyono, M.A.A. Aziz, A.F.A. Rahman, M.Y. S. Hamid, S.M. Izan, M.G.M. Nawawi, Chem. Eng. Sci. 193 (2019) 217–229.
- [41] K.S.W. Sing, Pure Appl. Chem. 57 (1985) 603–619.
- [42] M. Aravinthraj, F.L.A. Khan, J. Udayaseelan, A.A. Fernandes, Mater. Today. Proc. 47 (2021) 4391–4395.
- [43] G. Toscano, V. Maceratesi, E. Leoni, P. Stipa, E. Laudadio, S. Sabbatini, Fuel 313 (2022), 123017.
- [44] S. De Santis, F. Porcelli, G. Sotgiu, A. Crescenzi, A. Ceccucci, M. Verri, M. Caricato, C. Taffon, M. Orsini, Biochim. Biophys. Acta (BBA) - Mol. Basis Dis. 1868 166279 (2022).
- [45] Q. Shen, Y.-J. Fan, W.-M. Zhang, B.-L. Zhu, R. Wang, Z.-X. Sun, Chin. Chem. Lett. 26 (2015) 193–196.
- [46] F.L.R. Silva, A.A.A. Filho, M.B. da Silva, K. Balzuweit, J.-L. Bantignies, E.W. S. Caetano, R.L. Moreira, V.N. Freire, A. Righi, J. Raman Spectrosc. 49 (2018) 538–548.
- [47] A. Chandrasekar, S. Vasantha, N.L. Jagadeesan, S.N. Shankar, B. Pannerselvam, V.G. Bose, G. Arumugam, M. Shammugavel, Biocatal. Agric. Biotechnol. 33 (2021), 101994.
- [48] J.S. Elias, K.A. Stoerzinger, W.T. Hong, M. Risch, L. Giordano, A.N. Mansour, Y. Shao-Horn, ACS Catal. 7 (2017) 6843–6857.
- [49] M. Ladan, W.J. Basirun, S.N. Kazi, F.A. Rahman, Mater. Chem. Phys. 192 (2017) 361–373.
- [50] F.A. Pearsall, J. Lombardi, S. O'Brien, ACS Appl. Mater. Interfaces 9 (2017) 40324–40332.
- [51] Q. Fu, M. Yang, Z. Liu, H. Yang, F. She, X. Zhang, F. Xie, Y. Hu, J. Chen, J. Colloid Interface Sci. 618 (2022) 161–172.
- [52] M.D. Hernández-Alonso, I. Tejedor-Tejedor, J.M. Coronado, M.A. Anderson, Appl. Catal. B: Environ. 101 (2011) 283–293.
- [53] A. Kowalczyk, A. Święs, B. Gil, M. Rutkowska, Z. Piwowarska, A. Borcuch, M. Michalik, L. Chmielarz, Appl. Catal. B: Environ. 237 (2018) 927–937.
- [54] M. Rutkowska, I. Pacia, S. Basaq, A. Kowalczyk, Z. Piwowarska, M. Duda, K. A. Tarach, K. Góra-Marek, M. Michalik, U. Díaz, L. Chmielarz, Microporous Mesoporous Mater. 246 (2017) 193–206.
- [55] M.J. Climent, A. Corma, S. Iborra, K. Epping, A. Velty, J. Catal. 225 (2004) 316–326.
- [56] C. Yang, J. Wang, Q. Xu, Microporous Mater. 11 (1997) 261–268.
- [57] S. Bhandari, R. Khatun, M.K. Poddar, A.C. Kothari, R. Bal, Mol. Catal. 528 (2022), 112473.
- [58] W.H. Yu, B. Zhu, D.S. Tong, K. Deng, C.P. Fu, T.H. Huang, C.H. Zhou, Clays Clay Miner. (2022).
- [59] A.K. Singh, Q. Xu, ChemCatChem 5 (2013) 652–676.
- [60] T. Wigmans, J.A. Moulijn, J. Chem. Soc., Chem. Commun. (1980) 170–171.
- [61] P. Mohanty, M. Patel, K.K. Pant, Bioresour. Technol. 123 (2012) 558–565.
- [62] T. Wei, M. Wang, W. Wei, Y. Sun, B. Zhong, Fuel Process. Technol. 83 (2003) 175–182.
- [63] T. Uchijima, Catal. Today 28 (1996) 105–117.
- [64] F. Bertella, P. Concepción, A. Martínez, Catal. Today 289 (2017) 181–191.
- [65] N.D. Charisiou, K.N. Papageridis, L. Tzounis, V. Sebastian, S.J. Hinder, M.A. Baker, M. AlKetbi, K. Polychronopoulou, M.A. Goula, Int. J. Hydrog. Energy 44 (2019) 256–273.
- [66] F. Frusteri, S. Freni, L. Spadaro, V. Chiodo, G. Bonura, S. Donato, S. Cavallaro, Catal. Commun. 5 (2004) 611–615.
- [67] C.-S. Wu, R. Li, Q.-Q. Wang, L. Yang, Green. Chem. 21 (2019) 269–274.
- [68] X. Zhang, L. Wang, Green. Chem. 14 (2012) 2141–2145.
- [69] J. Wu, T. Chen, X. Luo, D. Han, Z. Wang, J. Wu, Waste Manag. 34 (2014) 676–682.
- [70] A. Marcilla, M.I. Beltrán, R. Navarro, J. Anal. Appl. Pyrolysis 76 (2006) 222–229.
- [71] J. Li, X. Yao, S. Chen, K. Xu, B. Fan, D. Yang, L. Geng, H. Qiao, Process Saf. Environ. Prot. 160 (2022) 341–353.
- [72] S.-F. Jiang, G.-P. Sheng, H. Jiang, ACS Sustain. Chem. Eng. 7 (2019) 12639–12655.
- [73] H. Xin, J. Sun, L. Zhang, W. Tian, B. Zhou, Z. Tang, X.-Y. Qi, C. Di, X. Zhong, D.-M. Wang, ACS Omega 6 (2021) 20846–20854.
- [74] S.A. Rub Pakkath, S.S. Chetty, P. Selvarasu, A. Vadivel Murugan, Y. Kumar, L. Periyasamy, M. Santhakumar, S.R. Sadras, K. Santhakumar, ACS Biomater. Sci. Eng. 4 (2018) 2582–2596.
- [75] J. Li, B. Dou, H. Zhang, H. Zhang, H. Chen, Y. Xu, J. Environ. Chem. Eng. 9 (2021), 105311.
- [76] J. Zhang, H. Zou, J. Liu, F. Evrendilek, W. Xie, Y. He, M. Buyukada, J. Hazard. Mater. 401 (2021), 123276.
- [77] H. Wang, H. Han, E. Sun, Y. Han, Y. Zhang, J. Li, Y. Chen, H. Song, H. Zhao, Y. Kang, Energy Fuels 33 (2019) 8596–8605.
- [78] R. Janu, V. Mrlik, D. Ribitsch, J. Hofman, P. Sedláček, L. Bielská, G. Soja, Carbon Resour. Convers. 4 (2021) 36–46.
- [79] S. Keerthan, S.M. Rajapaksha, L. Trakal, M. Vithanage, Environ. Res. 189 (2020), 109865.
- [80] P. Barczyński, M. Szafran, M. Ratajczak-Sitarz, Ł. Nowaczyk, Z. Dega-Szafran, A. Katrusiak, J. Mol. Struct. 1018 (2012) 21–27.
- [81] M. Szafran, A. Katrusiak, I. Kowalczyk, A. Komasa, Z. Dega-Szafran, J. Mol. Struct. 1017 (2012) 115–122.
- [82] R.L. Frost, L. Duong, M. Weier, Spectrochim. Acta Part A: Mol. Biomol. Spectrosc. 60 (2004) 1853–1859.
- [83] V.L. Furer, E.I. Borisoglebskaya, V.V. Zverev, V.I. Kovalenko, Spectrochim. Acta Part A: Mol. Biomol. Spectrosc. 63 (2006) 207–212.
- [84] S.J. Gregg, K.S.W. Sing, H.W. Salzberg, J. Electrochem. Soc. 114 (1967) 279C.

[85] Y.-G. Guo, H.-M. Zhang, J.-S. Hu, L.-J. Wan, C.-L. Bai, *Thin Solid Films* 484 (2005) 341–345.

[86] Z. Wang, Y. Zhang, E.C. Neyts, X. Cao, X. Zhang, B.W.L. Jang, C.-J. Liu, *ACS Catal.* 8 (2018) 2093–2110.

[87] Y. Wang, M. Craven, X. Yu, J. Ding, P. Bryant, J. Huang, X. Tu, *ACS Catal.* 9 (2019) 10780–10793.

[88] A.A. Kamnev, A.V. Tugarova, Y.A. Dyatlova, P.A. Tarantilis, O.P. Grigoryeva, A. M. Fainleib, S. De Luca, *Spectrochim. Acta Part A: Mol. Biomol. Spectrosc.* 193 (2018) 558–564.

[89] A. Singh, V. Goyal, J. Singh, H. Kaur, S. Kumar, K.M. Batoo, J. Gaur, M. Pal, M. Rawat, S. Hussain, *J. Clean. Prod.* 343 (2022), 131026.

[90] N. Patel, K.P. Shadangi, P.K. Kar, *Mater. Today.: Proc.* 38 (2021) 2866–2870.

[91] I. Fikri, M. El Amraoui, M. Haddad, A.S. Ettahiri, C. Falguères, L. Bellot-Gurlet, T. Lamhasni, S. Ait Lyazidi, L. Bejjit, *Spectrochim. Acta Part A: Mol. Biomol. Spectrosc.* 280 (2022), 121557.

[92] J.J. Ternero-Hidalgo, M.O. Guerrero-Pérez, J. Rodríguez-Mirasol, T. Cordero, M. A. Bañares, R. Portela, P. Bazin, G. Clet, M. Daturi, *Anal. Chem.* 92 (2020) 5100–5106.

[93] J.L. Reyes-Rodríguez, A. Velázquez-Osorio, D. Bahena-Uribe, A.B. Soto-Guzmán, M.A. Leyva, A. Rodríguez-Castellanos, S. Citalán-Cigarroa, O. Solorza-Feria, *Catal. Sci. Technol.* 9 (2019) 2630–2650.

[94] S. Zzeyani, M. Mikou, J. Naja, L. Bouyazza, G. Fekkar, M. Aiboudi, *Energy* 180 (2019) 206–215.

[95] A.M. Chibiryaev, I.V. Kozhevnikov, A.S. Shalygin, O.N. Martyanov, *Energy Fuels* 32 (2018) 2117–2127.

[96] A. Žužić, A. Ressler, J. Macan, *Solid State Commun.* 341 (2022), 114594.

[97] X. Yang, C. Tong, G. Chen, Y. Zhang, B. Jin, *Int. J. Coal Prep. Util.* (2022) 1–29.

[98] W. Wang, C. Duong-Viet, H. Ba, W. Baaziz, G. Tuci, S. Caporali, L. Nguyen-Dinh, O. Ersen, G. Giambastiani, C. Pham-Huu, *ACS Appl. Energy Mater.* 2 (2019) 1111–1120.

[99] A. Tanksale, F.L. Chan, *Biomass gasification using reactive flash volatilization technology*, RIRDC, 2014.